Friedrich-Alexander-Universität
Naturwissenschaftliche Fakultät

Master's Thesis
in Physics

Neutrino Event Simulation and Reconstruction for Water-Cherenkov Detectors

Franziska Kirchner

Supervisor: Prof. Dr. Claudio Kopper

Erlangen Centre for Astroparticle Physics

Submission date: 7 July 2026

Abstract

Neutrinos are elementary particles that due to their small cross-section can retain their original energy and direction over long distances. As such, they are useful messenger particles, providing information on their sources of origin. They can only be detected indirectly, e.g. with the use of water-Cherenkov detectors. Those neutrino detectors are typically built with instrumentation strings placed on a triangular grid. Next-generation detectors such as P-ONE or IceCube-Gen2 are planned as less ordered structures in order to optimize the detection of different high-energy neutrino topologies. However, it is not fully understood which detector geometries result in an optimal resolution of event energies or event positions. This thesis aims to provide a toy simulation that facilitates investigating the potential resolution of various detector configurations. Specifically, we simulate detectors and cascade events in their vicinity and determine the photon propagation from the events to the detection units. Then, the event energy and position can be reconstructed to investigate the resolution of different detectors.

Contents

1 Introduction

Neutrinos are a type of elementary particle in the Standard Model of physics. They naturally appear in radioactive decays, thus originating from nuclear fusion processes in the sun, but also from supernovae and their remnants, as well as from the Earth's atmosphere, triggered by highly energetic particle interactions (Vitagliano et al., 2020). Additionally, neutrinos also emerged right after the Big Bang, resulting in low-energy neutrinos permeating the cosmos and thus also named the Cosmic Neutrino Background (CNB) (Scott, 2024; Dey, 2024). Since according to the Standard Model, neutrinos only interact via the weak interaction, they travel through space mostly without interferences. This means that the information neutrinos carry about their source of origin via their energy and trajectory is mostly undisturbed. As such, they are a valuable asset in the search to expand our knowledge of the universe. To be precise, their unchanged trajectories, drawing a straight line between their point of origin and the Earth, make them ideal particles for the search of neutrino sources with new physics.

However, due to them not carrying electromagnetic charge and generally their small interaction probability, neutrino detection is only possible indirectly by detecting other particles resulting from their interaction. One method makes use of transparent, dielectric media, e.g., water or ice, to detect Cherenkov light produced by secondary particles from neutrino interactions. Water-Cherenkov detectors are able to measure the amount of Cherenkov light in large bodies of water and to reconstruct the energy and direction of travel of the initial neutrino the interaction was caused by. Current examples of such detectors include IceCube at the South Pole, which received an upgrade recently (King-Klemperer, 2026), and KM3Net in the Mediterranean Sea, which is still under construction but also already in use (KM3NeT Collaboration, 2025).

These current neutrino detectors have their limitations with their number and position of detection modules already determined. Hence, the resolution of an existing detector can only be improved by accumulating more statistics, an effect whose impact slows down over time, or by adding more detection modules over the course of the detector's lifetime. Additionally, the shapes chosen for those detectors were based on triangular grids when viewing the detection lines from above. Despite them being generally effective, they are not optimal configurations for some highly-specific scenarios that became apparent only after the current neutrino detectors were already built. These include the detection of ultra-high-energy neutrinos. Thus, future detector or upgrades to present detectors allow implementing geometries that further improve the resolution of certain detection events with respect to their energy or direction of travel. While a good knowledge of the energy is important to investigate diffuse fluxes and nearby sources, a good directional resolution is significantly better for researching far-away point sources.

Before implementing such improved geometries, it is first necessary to investigate what detector shapes might be optimal depending on what event types or event properties one prefers to investigate further. This is imperative as even when constructing a completely new detector with theoretically unlimited freedom of placement, one is still bound by financial and technical limits. For instance, such a project can only finance a certain number of Digital Optical Modules (DOMs) and their placement is constrained by how they can be held in place, especially when the detector site is an ocean. Additionally, all DOMs need some mean of transporting information, such as how many photons were registered from which directions at any moment. This is realized by cables connecting

all DOMs within a string and transporting all information to a central unit on the surface above the detector (for IceCube) (IceCube Collaboration, n.d.) or on the shore (for KM3Net) (KM3NeT Collaboration, n.d.). Those cables themselves have weight and a certain cost per meter of cable and thus cannot be used limitlessly either.
Hence, before constructing a full detector, one first needs to investigate different possible detector geometries and weigh their benefits like improved resolution for event energies or directions with their downsides such as the financial costs to then select a shape balancing those factors well. Comparing the resolutions can be done by simulating those detector geometries and various neutrino events and investigating how well those events can be detected by the differently-shaped detectors. For this, one can try to reconstruct the event properties from the number of photons detected at all of the DOMs and examine how well they corresponds to the initially simulated ones.
This thesis presents a simulation of neutrino detection events and a reconstruction of their properties, namely the energy and the starting position, for several manually implemented detector configurations. As such, it provides a tool to compare several detectors of different shapes with respect to their effective volume or resolution regarding energy or position.
In the future, these methods could be developed further to compare many more geometries or they could be adapted to be fully differentiable so that the detector shape with the best angular resolution for determining the event direction can be found.
In the following Section 2, this thesis will first go over the theory of neutrinos, specifically their properties, usual interactions, and sources. This is followed by detailing the relevant neutrino detection methods and different observable types of events The theory chapter then concludes by discussing common event reconstruction methods and present and future detector experiments. Second, the methods we used for both my simulation and my event reconstruction are detailed in Section 3. Thereafter comes a presentation of how said methods are specifically implemented in the code in Section 4. Section 5 then discusses the results of the event reconstruction. The thesis concludes in Section 6 with remarks reiterating the results and discussing potential for future research.

2 Theory of Neutrinos and Their Detection

In the Standard Model of particle physics, there exist particles of spin $\frac{1}{2}$, which are called fermions, and those of spin 1, which are called bosons. Fermions are divided into leptons ($e^-, \mu^-, \tau^-, \nu_e, \nu_\mu, \nu_\tau$, and their corresponding anti-particles) and quarks (u, d, c, s, t, b, and their corresponding anti-particles). Meanwhile, bosons include interaction particles of the weak, electromagnetic, and strong force, i.e. the $W^\pm$ and Z^0 bosons, the photon γ, and the gluon g, respectively.

2.1 Neutrino Properties

Within the Standard Model, where the gravitational force is excluded, leptons solely interact via electromagnetic and weak interactions, though the former only applies to the charged leptons $e^\pm$, $\mu^\pm$, and $\tau^\pm$ while neutrinos do not carry charge. Here, the doublet (e^-, ν_e) forms the first generation of leptons, while (μ^-, ν_μ) belongs to the second, and (τ^-, ν_τ) constitutes the third generation.

Neutrinos, together with gamma rays, charged particles, and gravitational waves, are important messengers that emerge from cosmic sources like black holes, supernovae, or neutron stars and travel through space.

Neutrinos have a low cross-section, which means that they interact less often than other particles. This leads to most neutrinos not being averted from their trajectory. Hence, a lot of information, e.g., the direction of the corresponding neutrino source, can be extracted once their direction of motion during the detection process on Earth is reconstructed. This makes them a useful asset in the search of cosmic sources.

Beyond the Standard Model, neutrinos are barely affected by gravitational forces due to their low mass. The exact masses of all three types of neutrinos are not known but it is evident that they are massive. This is a result of the detected neutrino oscillation, where the neutrino type may change between its site of origin and that of its detection (Bellini et al., 2014). From this observation follows that the neutrino mass eigenstates and the flavor eigenstates are not equivalent. The Pontecorvo-Maki-Nakagawa-Sakata (PMNS) matrix parametrizes the mixing angles between neutrino flavor and mass eigenstates as well as a charge-parity violating phase (Giganti et al., 2018). From experimental results, we know that the three neutrino masses can be ordered in two possible hierarchies, either the normal mass ordering or the inverted ordering (Salas et al., 2018).

2.2 Interactions

Neutrinos only couple via the weak interaction when solely considering the Standard Model and thus neglecting gravitation. However, not every weak interaction includes neutrinos. For the weak interaction, one has to distinguish between a charged current and a neutral current interaction. The former couples to a $W^\pm$ boson, exchanges charge, and can change the flavor of a lepton or quark, while the latter couples to a Z^0 boson, maintains the flavor and does not exchange charge. Since the masses of the $W^\pm$ and the Z^0 bosons are by far the largest of all interaction bosons with $M_W = 80.4\,\mathrm{GeV}$ and $M_Z = 91.2\,\mathrm{GeV}$ (Navas et al., 2024), the propagator is proportional to $\frac{1}{q^2 - M_{W,Z}^2}$, so very small. Hence, the probability amplitude of the weak interaction amounts to

$$|\mathcal{M}| \propto \frac{1}{\left(q^2 - M_{W,Z}^2\right)^2} \overset{|q^2| \ll M_{W,Z}^2}{\approx} \frac{1}{M_{W,Z}^4},$$

which is the smallest of the three interactions in the Standard Model. Additionally, the range of the weak interaction is proportional to $\frac{1}{M_{W,Z}}$ and hence very small. This means that neutrinos only interact seldom within their lifetime.
Several types of reactions caused by the weak interaction where neutrinos are part of the resulting products are described in the following.
At low energies, the beta decay and the similar electron capture are the most prominent ones. They are described by the following equations.

$$\begin{aligned}
\beta^- : \quad & {}^A_Z X_N && \rightarrow {}^A_{Z+1}Y_{N-1} + e^- + \bar{\nu}_e \\
\beta^+ : \quad & {}^A_Z X_N && \rightarrow {}^A_{Z-1}Y'_{N+1} + e^+ + \nu_e \\
\epsilon \;\; : \quad & {}^A_Z X_N + e^- && \rightarrow {}^A_{Z-1}Y'_{N+1} \qquad\quad + \nu_e
\end{aligned}$$

At higher energies, deep-inelastic scattering becomes the dominating process with the four different types of interaction shown in Figure 1. For charged current interactions, a neutrino scatters with a nucleon, exchanging a W boson and resulting in a hadronic jet and a highly energetic lepton of the same generation as the initial neutrino. A resulting high-energy $e^\pm$ can then interact further, causing an electromagnetic shower. Meanwhile, a resulting $\mu^\pm$ can travel up to several kilometers before decaying into a hadronic shower given its lifetime of about 2 µs (Bailey et al., 1977). Therefore, it can be measured on Earth after emerging in the atmosphere. Contrarily, a $\tau^\pm$ produced by deep-inelastic scattering has such a short lifetime that it quickly decays into another hadronic shower.

2.3 Neutrino Sources

Figure 2 provides an overview of neutrino sources and their according fluxes and energies of outgoing neutrinos.
The highest flux of neutrinos, which coincidentally occurs at lowest energies, originates from the CNB – neutrinos created shortly after the Big Bang and still present throughout in the universe. The CNB is described further by Scott (2024), Dey (2024), and Vitagliano et al. (2020). Due to the abundance of β^+ decays in the nuclear fusion processes of the Sun, where protons are converted into neutrons, it also produces a plethora of electron neutrinos ν_e. Additionally, neutrinos are also produced by thermal processes in the Sun. Meanwhile, neutrinos can also be produced in the Earth's atmosphere by deep-inelastic scattering of cosmic rays with atmospheric nuclei. These interactions result in neutrinos and hadronic showers, as described in Section 2.2. Further neutrinos then appear during the hadronic showers. The IceCube data in Figure 2 refers to the detection of high-energy neutrinos of astrophysical origin, first described in IceCube Collaboration (2013). The according neutrino sources can be galactic or extra-galactic, though most are expected to be extra-galactic, including star-forming galaxies, gamma-ray burst, active galactic nuclei, and galaxy clusters. There, the neutrinos are produced by interactions of cosmic rays either in the source, in

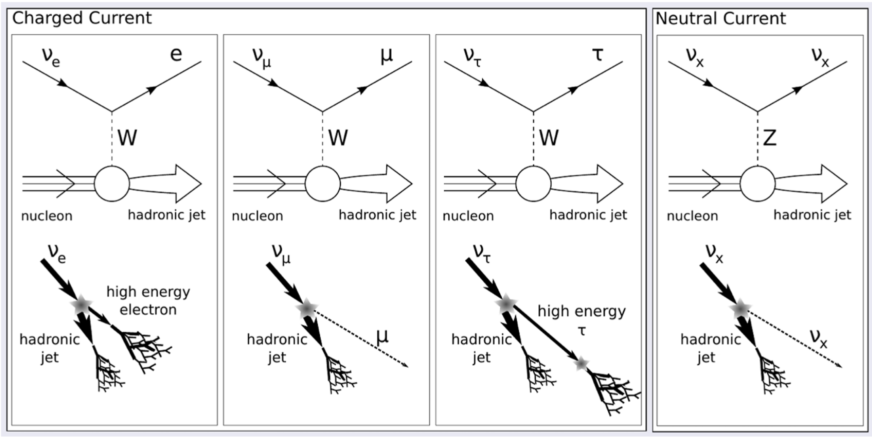

Figure 1: Types of Neutrino Interactions for Deep-Inelastic Scattering. Taken from Schneider (2024). For the charged current interaction, a neutrino of any flavor can interact with a nucleon by exchanging a $W^\pm$ boson, resulting in a hadronic jet and a charged lepton of the same generation. This outgoing charged lepton then decays into either an electromagnetic shower or another hadronic shower. Meanwhile, the interaction for the neutral current is the same for all lepton generations. Here, a neutrino scatters with a nucleon by exchanging a Z^0 boson, resulting in a hadronic jet and the same neutrino that initiated the scattering process.

its vicinity or on the trajectory of those rays to Earth. Additionally, ultra-high-energy neutrinos in the PeV to EeV range are associated with a "cosmogenic neutrino flux" and may originate from interactions of very high-energy cosmic rays.

2.4 Detection

Neutrinos can only be detected indirectly after triggering charged particles, which in turn may pass through a medium with refraction index n with a speed larger than the speed of light in the medium, so $v > c_n = \frac{c}{n}$. The charged particle then polarizes and excites particles in its surrounding medium which are then de-excited again while releasing photons into the medium. Normally, this process would result in the light spreading spherically. But since the charged particle is traveling at such a high speed, multiple instances of light wave fronts appear along the direction of travel of the particle in close succession. These multiple consecutive sources, which appear with a speed larger than the speed of light in the medium, the result in the individual light waves overlap into a cone of Cherenkov light as shown in Figure 3. This Cherenkov light can then be detected and its shape and trajectory can provide information about the charged particle, namely its energy and direction of travel.
For this thesis, the focus lies on neutrino detection in large bodies of water, where several types of neutrinos can interact with neutrons within H_2O molecules into the according lepton counterpart of the same lepton generation and a proton. Similarly, antineutrinos can interact with H_2O protons into the anti-lepton counterparts and neutrons.
For the detection of the Cherenkov light, one typically uses photomultiplier tubes (PMTs). Here, an incoming photon reaches a photocathode, where due to the photoelectric effect,

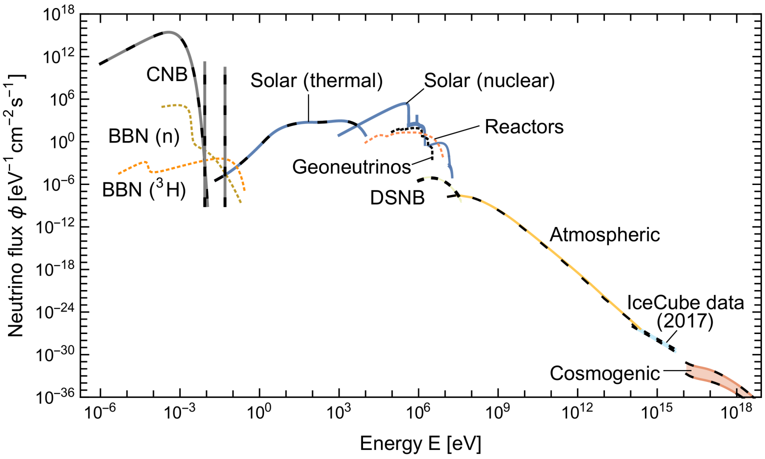

Figure 2: Different Neutrino Sources Depending on Neutrino Flux and Energy. Taken from Vitagliano et al. (2020). It shows the so-called Grand Unified Neutrino Spectrum arriving at Earth for all flux directions and all neutrino flavors together. Sources emitting only neutrinos are depicted with solid lines, while those producing solely antineutrinos appear as dashed or dotted lines. The lines composed of both solid and dashed lines are for sources of both neutrinos and antineutrinos.

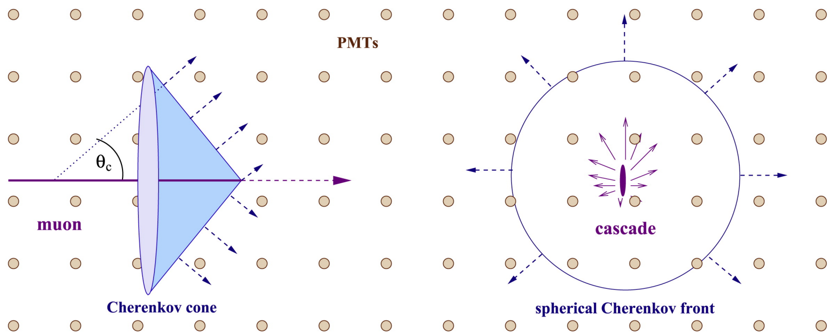

Figure 3: Cherenkov Light Cone of a Muon Track and a Cascade Event. Taken from Katz and Spiering (2012). For the muon track on the left, the muon speed larger than the speed of light in the medium results in a Cherenkov cone produced behind the muon. For the cascade event on the right, the Cherenkov light propagates spherically.

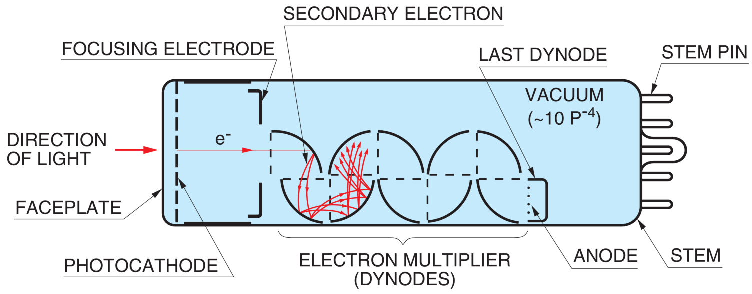

Figure 4: Illustration of a Photomultiplier Tube. Taken from Hamamatsu Photonics (n.d.). Light with a certain energy enters the vacuum tube on the left when arriving at the photocathode. There, it excites electrons on the material, which emits photoelectrons with an energy proportional to the energy of the incoming light. These electrons are then accelerated and focused toward the electrode. Thereafter, they reach the first dynode, where each incoming electron causes the emission of several secondary electrons. Hence, the number of electrons after the first dynode is a multiple of the number of electrons released by the photocathode. Then, the electrons pass several more dynodes, each one multiplying the number of electrons. The anode then registered the electrons, with the total charge proportional to the energy of the originally incoming light.

an electron with an energy proportional to the original photon's energy is excited and released into a vacuum tube permeated by an electric field. There, the electron is accelerated towards a first dynode, which in turn releases multiple secondary electrons. These then propagate towards the next dynode, for which the number of secondary electrons is again a multiple of the number of primary electrons. After passing through several dynodes, the total number of electrons is many times the amount of electrons released by the photocathode. Lastly, an anode collects all electrons, their total charge being proportional the energy of the originally detected photon.
In practice, several of those PMTs are set up on a single DOM so that they are all focused on different directions. Many of those DOMs are connected on a single detection line, and many of those are all set up vertically in a body of water or ice to together form a whole detection array or detector.

2.5 Event Types

High-energy cosmic neutrinos predominantly interact via deep-inelastic scattering as described in Section 2.2. There, for both a charged current and a neutral current interaction, the neutrino scatters with a nucleon, which results in a shower of hadronic particles and an outgoing neutrino or charged lepton. Both an outgoing $e^{\pm}$ and $\tau^{\pm}$ then quickly decay further into a secondary shower of electromagnetic or hadronic particles, respectively. Hence, when a cosmic neutrino interacts in water at a detection site, those particle showers are detected as many photons propagating radially outwards from the position of initial neutrino interaction. An example of such a cascade event detection is depicted in Figure 5a.
For the deep-inelastic scattering of ν_μ specifically, the outgoing $\mu^{\pm}$ can pass distances up to several kilometers before also decaying into a hadronic shower. As such, a muon registered by a neutrino telescope on Earth can emerge in the water as a result of such

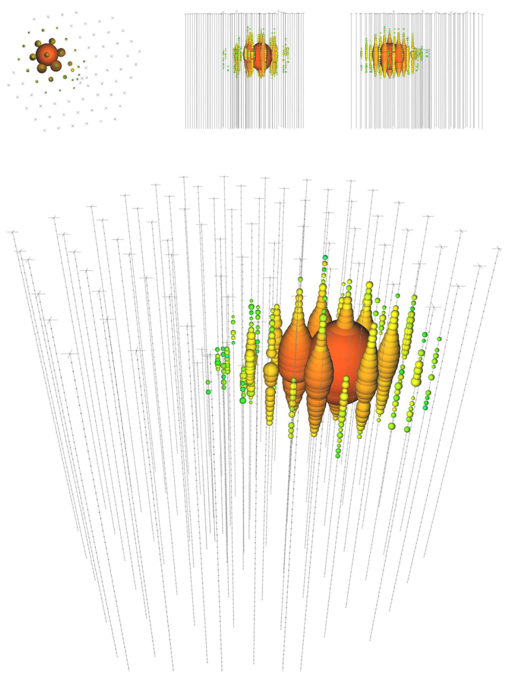

(a) Cascade Event that Deposited 1041 TeV in the Detector.

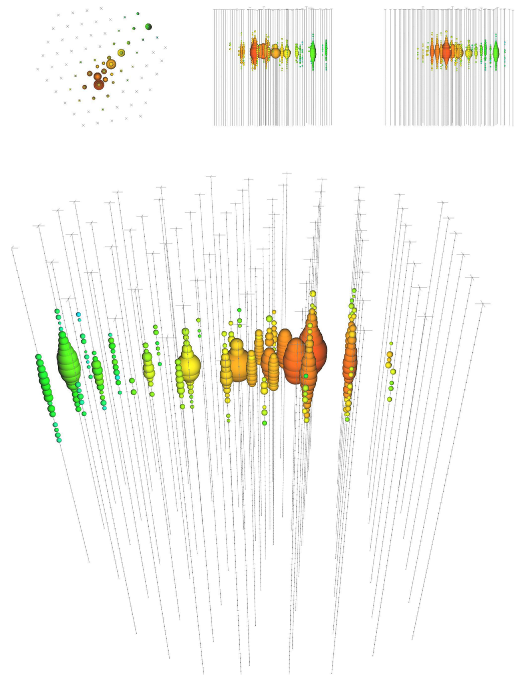

(b) Muon Track Event that Deposited 71 TeV in the Detector.

Figure 5: Examples of Neutrino Events as Measured in the IceCube Neutrino Detector. Taken from IceCube Collaboration (2013). Figure 5a depicts a cascade event, while Figure 5b shows an exemplary muon track event. For each, the three smaller figures at the top are a top-down and two side views, corresponding to projections to the x-, y-, and z-axes of the detector. The larger figures at the bottom constitute three-dimensional displays. Each sphere correspond to one DOM involved in the event detection, with the size correlating to the amount of photons measured by the module. The sphere colors encode the photon arrival time after the event emergence, ranging from 0 µs for dark red to 4 µs for cyan.

an interaction of a cosmic neutrino. Alternatively, the muon can also originate from the atmosphere and hence be produced by an atmospheric neutrino. Tracks of high-energy muons are registered when they pass through the detector and continuously shed parts of their energy during their trajectory. Whenever a part of the energy is deposited, a small cascade of secondary particles is produced and through these, the whole muon trajectory can be tracked. It is not a given that the the muon is produced within the detector or fully decays within it. On the contrary, many muon tracks emerge before entering the detection volume and continue far beyond that, with only a fraction of the full muon energy being deposited in the detector. Figure 5b shows an exemplary muon track detection.

For the simulation presented in this thesis, we a priori distinguish between cascade and muon track topologies as they are fundamentally different events in the investigated energy range.

2.6 Current and Future Experiments

A type of high-energy neutrino telescope that uses water as the detection medium are water-Cherenkov neutrino telescopes.
One of those is IceCube, is a cubic-kilometer neutrino detector situated at the South Pole within the Antarctic ice sheet. It includes a section of higher string density in its center called DeepCore that extends its sensitivity to lower-energy neutrinos. An upgrade that extended the number of strings was finished this year (King-Klemperer, 2026). A full extension towards IceCube-Gen2 is planned for the future (IceCube-Gen2 Collaboration, 2023). The general IceCube setup is presented in Figure 6. KM3NeT is another example under construction in the Mediterranean sea. It consists of two detector parts, ARCA for high-energy neutrino detection, and ORCA with a higher sensor and string density for measuring low-energy neutrinos. While ARCA is situated off the coast of Sicily, ORCA is constructed near the French coast. Figure 7 shows the setup of the KM3NeT detector. The Pacific Ocean Neutrino Experiment (P-ONE) is another water Cherenkov neutrino detector for deployment in the Pacific off the coast of Canada. The first detection string has already been constructed, but not yet deployed. A potential detector setup is depicted in Figure 8.
This thesis investigates the effect of a detector configuration on its resolution and effective detection volume. In the future, the simulation and reconstruction code could even be translated into a fully-differentiable algorithm for automated optimization of some geometries with respect to their resolution. As such, this thesis may contribute to the finalization of future detectors configurations, e.g., P-ONE or IceCube-Gen2.

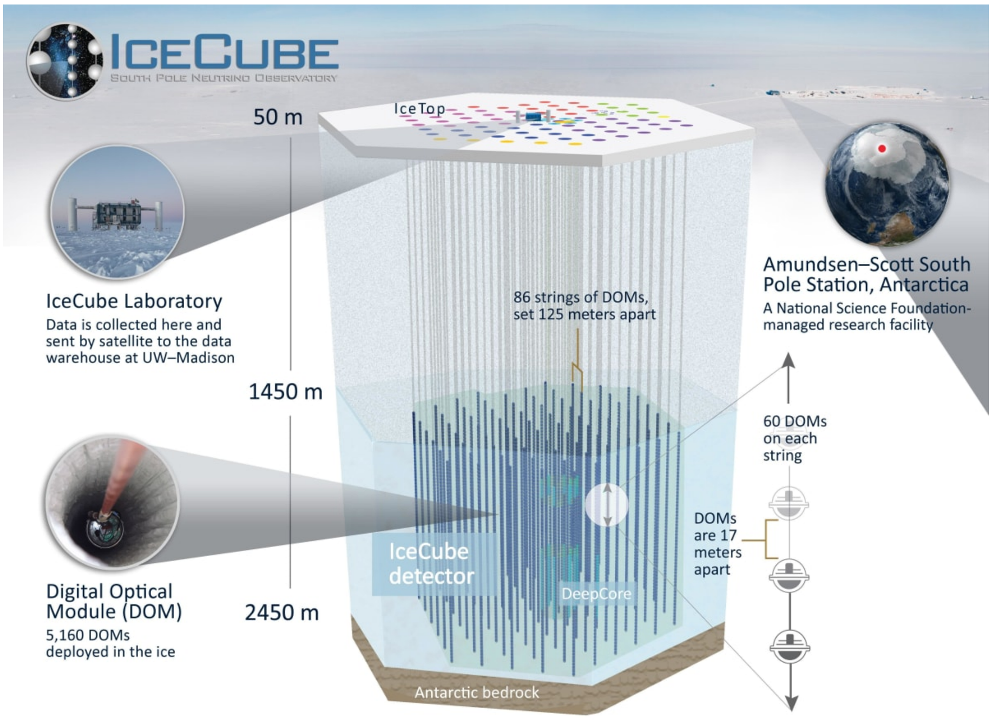

Figure 6: Setup of the IceCube Neutrino Detector. Taken from IceCube Collaboration (n.d.). The detector is situated at the South Pole. It is embedded in the Antarctic ice and encompasses many DOMs aligned vertically over a distance of 1 km on strings.

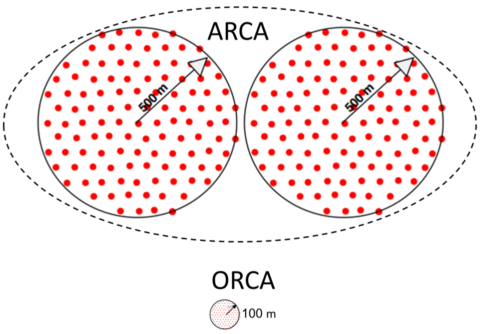

(a) Top View of the Complete KM3NeT Setup.

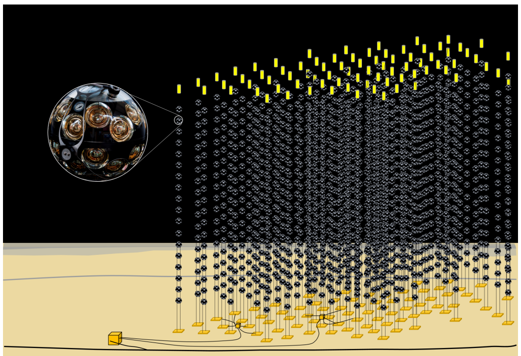

(b) Side View of One Detector Part.

Figure 7: Setup of the KM3NeT Neutrino Detector. Taken from KM3NeT Collaboration (n.d.). Figure 7a shows the top-down view of strings of the ARCA and the ORCA detector that together constitute the KM3NeT detector. Figure 7b shows the detection strings for one detector part, attached to the ocean floor and containing multiple DOMs each.

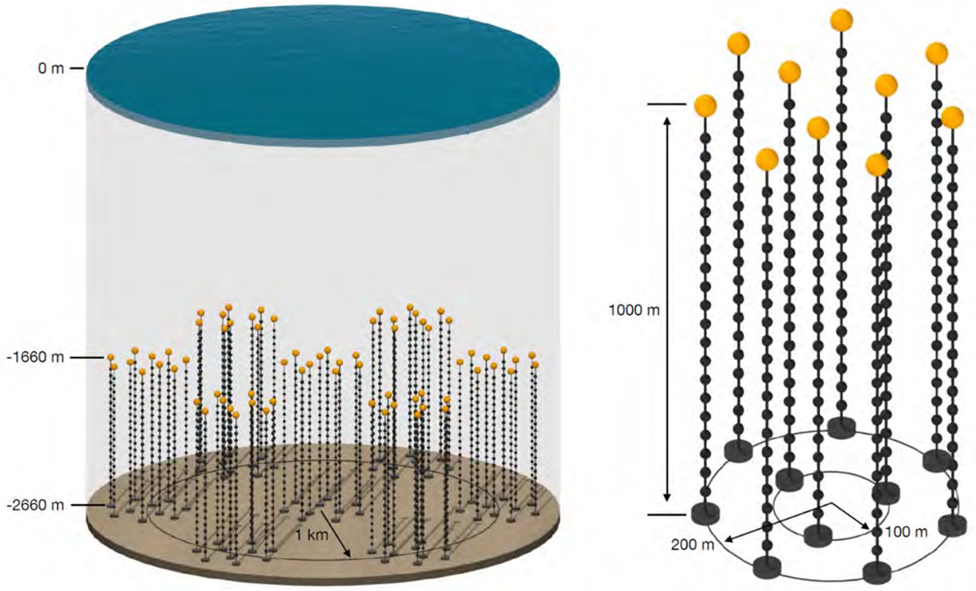

Figure 8: Planned Setup of the P-ONE Neutrino Detector. Taken from P-ONE Collaboration (2019). The strings with their DOMs are attached to the ocean floor and grouped into multiple partial detectors.

3 Methods

This sections presents the methods used for the event simulation and reconstruction for both the energy and the position of cascade events. An outlook on muon track events then concludes the chapter.

3.1 Simulation

To be able to quantify the correctness of the event energies determined by the detector, several events are simulated, and their energies are reconstructed and then compared to the original energies used for the simulation. Specifically, this is done as follows.

3.1.1 Basic Simulation Setup

At first, the detector modules are set up on several lines aligned vertically. For this simple reconstruction, we start with a cubic lattice detector where the total array lengths in the x- and y-direction are identical to the line length of 1 km. Later on, other shapes are considered as well and are the compared to the cubic detector. Figure 9 shows the setup of such a cubic detector with several DOMs on a detection string and those strings then aligned in the z-direction.
Then, cascade events are initialized with random energies sampled uniformly in the logarithm within [10^2 GeV; 10^6 GeV], drawing from [2; 6] and using the result as the power of 10. The positions are also random, with each position dimension sampled uniformly within the corresponding detector side length plus an additional border of 10% of each side length at both ends For the 1 km^3 detector, this means the volume containing both the detector and the border has a length, width, and height of 1.1 km, encompassing a cubic volume of 1.33 km^3. At those event positions, a neutrino of any type decays and results in a particle shower, also called a cascade, and photons being expelled radially outwards. This is an approximation of those cascade events measured in actual water-Cherenkov detectors. There, a true particle shower is subjected to a certain boost depending on the initial energy, leading to an asymmetrical photon spread. The simulated photons are then detected by PMTs on the DOMs. For a simplified simulation, we omit simulating optical properties of the PMTs like the detection efficiency or a limited detection angle less than the full solid angle, and instead, all DOMs are implemented to detect all photons that reach them. Still, a trigger threshold is implemented so that not all simulated events are detected. This threshold is currently set at ≥ 5 photons detected from one event by the complete detector
From this photon yield for all DOMs in the detector we can draw several samples from a Poisson distribution. This can be realized because the implemented photon yield corresponds to the expected mean photon yield at actual neutrino telescopes. Drawing several Poisson-distributed samples allows us to measure the same event multiple times with slightly different photon measurements due to statistics.
The measured number of detected photons at each DOM depends on the energy of the event, its distance to the module, and theoretically also the optical properties of the module, although the latter is not simulated here. The goal is then to reconstruct the energy and the position of the initial cascade event from the number of photons measured at all DOMs within the detector.

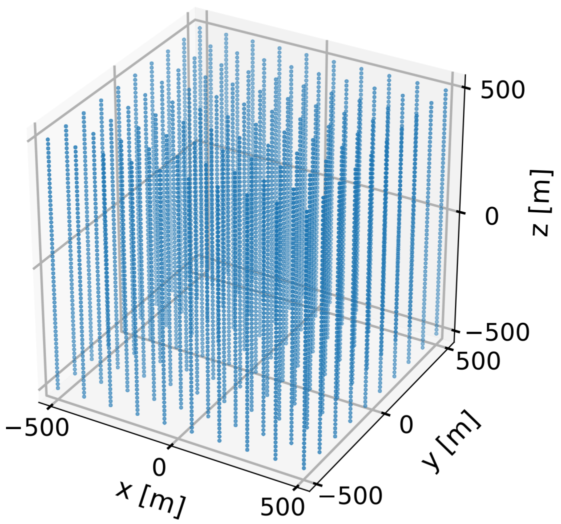

Figure 9: Setup of the Basic Neutrino Detector Used in Our Simulation. It consists of 10 by 10 strings on a square grid. Each string contains 60 DOMs and has a length of 1 km. The square surface area of the detector encompasses $1\,\mathrm{km}^2$, leading to a cubic detector spanning a volume of $1\,\mathrm{km}^3$.

Unless otherwise noted, the experiments are all undertaken with the cubic detector as depicted in Figure 9 with events initialized within the detector volume and the surrounding border volume.

Alternatively, we can also initialize all events in fixed volume significantly larger than the detector volume instead. The effective detection volume V_{eff} can then be determined from

$$V_{\mathrm{eff}} = V_{\mathrm{events}} \cdot \frac{N_{\mathrm{detected}}}{N_{\mathrm{initialized}}}, \tag{1}$$

where V_{events} is the volume spanned by the events. N_{detected} is the number of detected events, so all those passing the trigger threshold of ≥ 5 photons detected when summing over all DOMs. And $N_{\mathrm{initialized}}$ is the number of events initialized by the simulation. Equation 1 can be calculated as a total effective volume or for individual energy values so that an energy-dependent effective volume can be studied. In the future, this effective volume could even be determined for binned energies so that our results for discrete energy values could be confirmed for an extension to continuous inputs.

3.1.2 Photon Yield

The amount of photons that are released by a cascade event and measured at a single DOM is provided by the photon yield function for a point source presented in Aartsen et al. (2014), which amounts to

$$\mu(r) = n_0 A \frac{1}{4\pi} e^{\frac{-r}{\lambda_p}} \frac{1}{\lambda_c r \tanh\left(\frac{r}{\lambda_c}\right)}, \tag{2}$$

where

$$\begin{aligned}
\lambda_c &= \frac{\lambda_e}{3\zeta}, \\
\lambda_p &= \frac{\sqrt{\frac{\lambda_a \lambda_e}{3}}}{1.07}, \\
\zeta &= e^{-\frac{\lambda_e}{\lambda_a}}, \\
\lambda_e &= 24, \\
\lambda_a &= 98, \\
n_0 A &= 63894457.33843762.
\end{aligned}$$

Here, λ_a is the absorption length, λ_e the effective scattering length, and λ_p the characteristic propagation length, which depends on the former two lengths. The value for $n_0 A$ is the result of a curve fit realized by Mayer (2025).
It should be noted that this simulation does not include that in reality, PMTs have a different sensitivity for different wavelengths of light. Instead, the amount of measured photons presented here results from a weighted average of the wavelength sensitivity curve times the number of photons arriving at a DOM from the Cherenkov light cone. Since the data was fitted by Mayer (2025) specifically for an energy of 300 TeV and thus, for the energy-dependent photon number, Equation 2 needs to be re-normalized to the energy currently under consideration. This results in

$$\mu(r, E) = \mu(r) \cdot \frac{E\,[\mathrm{GeV}]}{3 \cdot 10^5\,\mathrm{GeV}} = n_0 A \frac{1}{4\pi} e^{\frac{-r}{\lambda_p}} \frac{1}{\lambda_c r \tanh\left(\frac{r}{\lambda_c}\right)} \cdot \frac{E\,[\mathrm{GeV}]}{3 \cdot 10^5\,\mathrm{GeV}}. \tag{3}$$

Figure 10 depicts a graphical illustration of the amount of photons released by an event over the distance to this event as presented in Equation 2, corresponding to the photon number detectable by a DOM depending on its position relative to the event position.

3.2 Reconstruction

This section discusses methods of reconstructing general event properties and estimation the reconstruction uncertainty. Then, we focus on the specific application on both energy and position reconstruction of cascade events

3.2.1 Reconstructing Event Properties

For a parameter reconstruction, the simplified photon propagation model receives both event energies and event positions as input and oen parameter is then reconstructed while the other is fixed at the known value. This reconstruction is done using the so-called maximum likelihood principle which states that the best estimate $\hat{\theta}$ of a parameter θ is that which maximizes the joint probability

$$L = \prod_{i}^{n} L_i = \prod_{i=1}^{n} f(X_i, \theta)$$

with respect to the given data X_i. The sum over n corresponds to a sum over photon numbers measured at individual DOMs. Here, L_i are also called likelihood functions

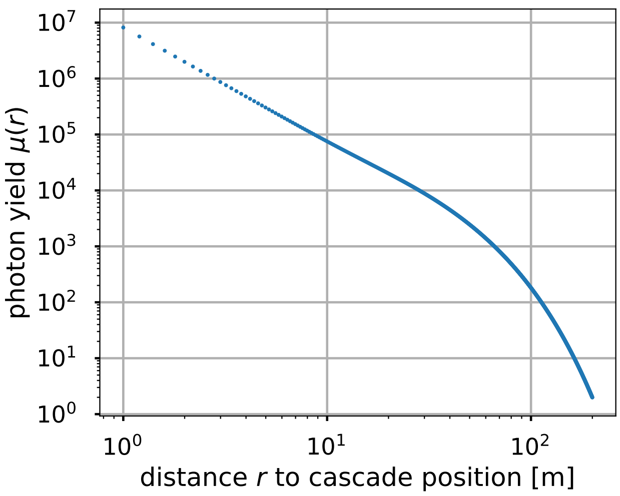

Figure 10: Measured Photon Yield of a Cascade Event Depending on the Distance to the Event Position. This is an illustration of Equation 3 for an energy of $E = 5 \cdot 10^5$ GeV. Initially, the photon yield decrease linearly in a double-logarithmic plot. After a distance of approximately 50 m from the event, the slope increases consecutively.

and refer to different detector modules, while L denotes the total likelihood function for one event sample.

Additionally, in our case here, the individual probability distributions f are all Poisson distributions

$$L_i = f(X = k|\lambda) = \frac{\lambda^k}{k!} e^{-\lambda}, \tag{4}$$

where λ is the expectation value of event numbers, and k_i is the measured number of events.

Hence, in this case the likelihood is calculated using

$$L = \prod_i^n L_i = \prod_{i=1}^n f(X = k|\lambda) = \prod_{i=1}^n \frac{\lambda^{k_i}}{k_i!} e^{-\lambda}, \tag{5}$$

where the expectation λ refers to the true photon yield $\mu(r, E)$ resulting from Equation 3 and k_i corresponds to a measurement sample of said photon yield at a single DOM, while the sum over i from $[1; n]$ is a sum over all DOMs.

This means the best estimate for the energy can be found at the maximum of the likelihood curve that is calculated from a product of the probability distributions for all individual DOMs. Numerically, it is preferred to calculate $\ln L$ instead of solely the likelihood function L by itself. This causes the results to be more numerically stable. Additionally, many algorithms are optimized for minimization operations instead of maximizing. Hence, we then minimize $-\ln L$ to receive estimates for event energies.

When calculating this negative logarithm of the total likelihood function, Equation 5 turns into

$$
\begin{aligned}
-\ln L &= -\ln\left(\prod_{i=1}^{n} L_i\right) \\
&= -\ln\left(\prod_{i=1}^{n} \frac{\lambda^{k_i}}{k_i!} e^{-\lambda}\right) \\
&= -\ln\left(\prod_{i=1}^{n} \frac{\lambda^{k_i}}{k_i!} e^{-\lambda}\right) \\
&= -\sum_{i=1}^{n} \ln\left(\frac{\lambda^{k_i}}{k_i!} e^{-\lambda}\right) \\
&= -\sum_{i=1}^{n} \Big(k_i \ln\left(\lambda\right) - \ln(k_i!) - \lambda\Big),
\end{aligned}
$$

arriving at

$$
\begin{aligned}
-\ln L &= -\ln\left(\prod_{i=1}^{n} L_i\right) \\
&= \sum_{i=1}^{n} \left(-\ln L_i\right) \qquad (6) \\
&= \sum_{i=1}^{n} \Big(-k_i \ln\left(\mu(r,E)\right) + \ln(k_i!) + \mu(r,E)\Big).
\end{aligned}
$$

3.2.2 Uncertainty Estimation

In addition to estimating the energy, we are also interested in a measurement for the estimation uncertainty σ.
One method uses that the 1σ interval is given by the distance between the parameter points $\vartheta_{1,2}$ for which

$$-\ln L(\vartheta_{1,2}) = -\ln L(\vartheta_{min}) + \frac{1}{2}$$

holds. This is an adaptation of the original equation presented in Lista (2023) where the uncertainty interval is determined by the points $\theta_{1,2}$ solving

$$-2\ln L(\theta_{1,2}) = -2\ln L_{\max} + 1.$$

In other words, the length of a horizontal line at $\frac{1}{2}$ above the likelihood curve minimum that connects both sides of the parabola-like logarithmic curve corresponds to the interval between $[\vartheta_{min} - 1\sigma, \vartheta_{min} + 1\sigma]$. An illustration for this method applied to the energy reconstruction is depicted in Figure 11.
An alternative measurement for the uncertainty estimation is given by the Fisher Information since according to the Cramér-Rao bound (Cramér, 1946), the uncertainty is limited by the Fisher Information of the likelihood function L via

$$\sigma \geq \frac{1}{\sqrt{\mathcal{F}}}. \qquad (7)$$

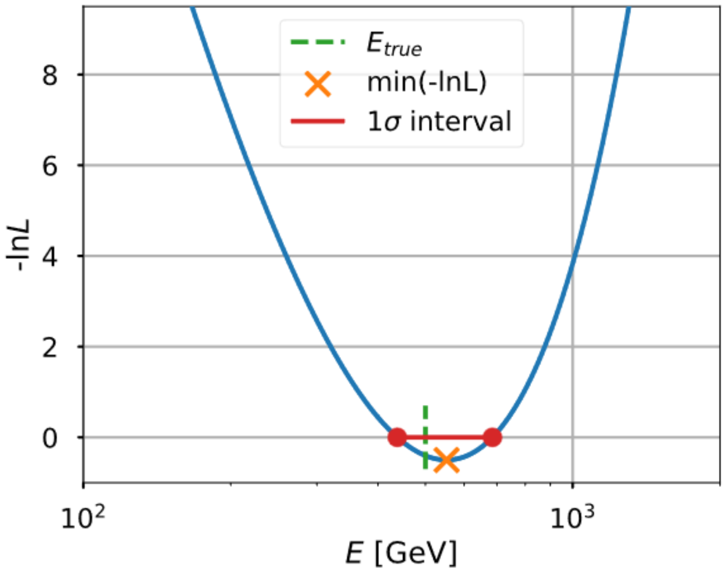

Figure 11: Illustration of the Log-Likelihood Minimization Process as Described in Section 3.2.2. It depicts the log-likelihood curve of a single cascade event over the energy. The curve minimum corresponds to the reconstructed energy value. The displayed minimum lies at $-\frac{1}{2}$ because we subtract first the curve minimum and then this additional value of $-\frac{1}{2}$ from the log-likelihood. As a result, the width between both roots of the curve constitutes the 1σ uncertainty interval. We expect this interval to contain the true energy value as initialized in the simulation approximately 68% of the time.

In general, the Fisher Information matrix element $\mathcal{F}_{ij}$ for a function f depending on a dataset X_n and the parameters ϑ_i and ϑ_j is calculated as

$$\mathcal{F}_{ij} = \mathbb{E}\left[\left(\frac{\partial}{\partial\vartheta_i}\ln f(X_n|\vartheta_i)\right)\cdot\left(\frac{\partial}{\partial\vartheta_j}\ln f(X_n|\vartheta_j)\right)\right], \tag{8}$$

where $\mathbb{E}$ denotes the expectation value and ∂ is the partial derivative.
However, when there is only a single parameter we want to optimize, we arrive at the special case $i = j = 1$ so that the single matrix element $\mathcal{F}_{11}$ represents the whole Fisher Information result

$$\mathcal{F} = \mathbb{E}\left[\left(\frac{\partial}{\partial\vartheta}\ln f(X_n|\vartheta)\right)^2\right], \tag{9}$$

When it is known that the underlying probability distributions that comprise the likelihood function are all Poisson distributions $f(X = k|\lambda)$ according to Equation 4, the Fisher Information can be simplified to

$$\begin{aligned}
\mathcal{F}_{i,j}(\lambda(\vartheta)) &= \mathbb{E}\left[\left(\frac{\partial}{\partial\vartheta_i}\ln f(k|\lambda)\right)\cdot\left(\frac{\partial}{\partial\vartheta_j}\ln f(k|\lambda)\right)\right]\\
&= \mathbb{E}\left[\left(\frac{\partial}{\partial\lambda}\ln f(X = k|\lambda)\frac{\partial\lambda}{\partial\vartheta_i}\right)\cdot\left(\frac{\partial}{\partial\lambda}\ln f(X = k|\lambda)\frac{\partial\lambda}{\partial\vartheta_j}\right)\right]\\
&= \mathbb{E}\left[\left(\frac{\partial}{\partial\lambda}\ln f(X = k|\lambda)\right)^2\frac{\partial\lambda}{\partial\vartheta_i}\frac{\partial\lambda}{\partial\vartheta_j}\right]\\
&= \mathbb{E}\left[\left(\frac{\partial}{\partial\lambda}(k\ln(\lambda) - \ln(k!) - \lambda)\right)^2\frac{\partial\lambda}{\partial\vartheta_i}\frac{\partial\lambda}{\partial\vartheta_j}\right]\\
&= \mathbb{E}\left[\left(\frac{k}{\lambda} - 1\right)^2\right]\cdot\frac{\partial\lambda}{\partial\vartheta_i}\frac{\partial\lambda}{\partial\vartheta_j}\\
&\overset{\mathbb{E}(X)=\lambda}{=} \mathbb{E}\left[\left(\frac{k}{\lambda} - \frac{\mathbb{E}(X)}{\lambda}\right)^2\right]\cdot\frac{\partial\lambda}{\partial\vartheta_i}\frac{\partial\lambda}{\partial\vartheta_j}\\
&\overset{k=\sum_i k_i=\sum_i X_i=X}{=} \mathrm{Var}\left(\frac{X}{\lambda}\right)\cdot\frac{\partial\lambda}{\partial\vartheta_i}\frac{\partial\lambda}{\partial\vartheta_j}\\
&= \frac{\mathrm{Var}(X)}{\lambda^2}\cdot\frac{\partial\lambda}{\partial\vartheta_i}\frac{\partial\lambda}{\partial\vartheta_j}\\
&\overset{\mathrm{Var}(X)=\lambda}{=} \frac{\lambda}{\lambda^2}\cdot\frac{\partial\lambda}{\partial\vartheta_i}\frac{\partial\lambda}{\partial\vartheta_j}\\
&= \frac{1}{\lambda}\cdot\frac{\partial\lambda}{\partial\vartheta_i}\frac{\partial\lambda}{\partial\vartheta_j},
\end{aligned}$$

so that

$$\mathcal{F}_{ij} = \frac{1}{\lambda}\cdot\frac{\partial\lambda}{\partial\vartheta_i}\cdot\frac{\partial\lambda}{\partial\vartheta_j}. \tag{10}$$

In the case of a single parameter $\vartheta_i = \vartheta_j = \vartheta$ to be optimized, Equation 10 is transformed into

$$\mathcal{F}(\lambda(\vartheta)) = \frac{1}{\lambda}\cdot\left(\frac{\mathrm{d}\lambda}{\mathrm{d}\vartheta}\right)^2. \tag{11}$$

3.2.3 Application to Energy Reconstruction

When applying the calculation of the negative log-likelihood to the energy reconstruction, we can insert Equation 6 into Equation 9 with the single investigated parameter being the energy, so $\vartheta = E$, and the function we calculate the Fisher Information for is $-\ln L$. It should be noted that in general, it is irrelevant whether we insert $\ln L$ or $-\ln L$ into the equations as the minus sign then appears twice and they cancel each other out. Additionally, we can then take advantage of the fact that the photon yield of Equation 3 as it appears in the likelihood function only depends linearly on the energy, so

$$\frac{\partial \mu(r, E)}{\partial E} = \frac{\mu(r, E)}{E}.$$

Using all this information, we can determine the Fisher Information for the energy reconstruction in its general form thusly.

$$\begin{aligned}
\mathcal{F} &= \mathbb{E}\left[\left(\frac{\mathrm{d}\ln L}{\mathrm{d}E}\right)^2\right] \\
&= \mathbb{E}\left[\left(\frac{\mathrm{d}}{\mathrm{d}E}\sum_{i=1}^{n}\Big(-k_i \ln\big(\mu(r,E)\big) + \ln(k_i!) + \mu(r,E)\Big)\right)^2\right] \\
&= \mathbb{E}\left[\left(\sum_{i=1}^{n}\Big(-\frac{\mathrm{d}}{\mathrm{d}E}k_i \ln\big(\mu(r,E)\big) + \frac{\mathrm{d}}{\mathrm{d}E}\mu(r,E)\Big)\right)^2\right] \\
&= \mathbb{E}\left[\left(\sum_{i=1}^{n}\Big(-\frac{k_i}{\mu(r,E)} \cdot \frac{\partial \mu(r,E)}{\partial E} + \frac{\partial \mu(r,E)}{\partial E}\Big)\right)^2\right] \\
&\overset{\frac{\partial \mu(r,E)}{\partial E} = \frac{\mu(r,E)}{E}}{=} \mathbb{E}\left[\left(\sum_{i=1}^{n}\Big(-\frac{k_i}{\mu(r,E)} \cdot \frac{\mu(r,E)}{E} + \frac{\mu(r,E)}{E}\Big)\right)^2\right] \\
&= \mathbb{E}\left[\left(\sum_{i=1}^{n}\Big(-\frac{k_i}{E} + \frac{\mu(r,E)}{E}\Big)\right)^2\right],
\end{aligned}$$

hence

$$\mathcal{F} = \mathbb{E}\left[\left(\sum_{i=1}^{n}\Big(-\frac{k_i}{E} + \frac{\mu(r,E)}{E}\Big)\right)^2\right]. \tag{12}$$

Additionally, the simplified calculation as established in Equation 11 can be applied to the energy reconstruction in a similar manner by inserting into said equation the correspondence $\lambda = \mu(r, E)$ and using the relevant parameter $\vartheta = E$. Furthermore, we will once again make use of the linearity of $\mu(r, E)$ with respect to E. This results in

$$\mathcal{F} = \frac{1}{\mu(r,E)} \cdot \left(\frac{\partial \mu(r,E)}{\partial E}\right)^2 \overset{\frac{\partial \mu(r,E)}{\partial E} = \frac{\mu(r,E)}{E}}{=} \frac{1}{\mu(r,E)} \cdot \left(\frac{\mu(r,E)}{E}\right)^2. \tag{13}$$

3.2.4 Comparison of Different Detector Configurations

The energy reconstruction and specifically the corresponding uncertainties can be compared for different grid shapes and string densities.

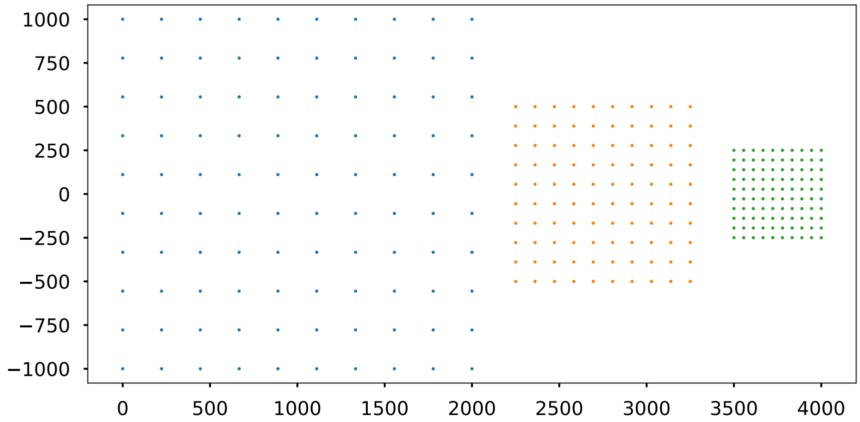

Figure 12: Surface Area Comparison of Three Detectors with Square Surfaces. All three consist of 10×10 strings ordered in a square grid. The largest configuration has a side length of 2000 m, the medium one one of 1000 m, while the smallest one is constrained to a length of 500 m. The height of 1000 m is equivalent for all three detectors. In any simulation run, only one of these detectors is initialized at once with the coordinate system center coinciding with the detector center.

For one, we can compare three detectors containing 10×10 strings each. One detector is spread out over an area of $1000\,\mathrm{m} \times 1000\,\mathrm{m}$, and the others over areas of $500\,\mathrm{m} \times 500\,\mathrm{m}$ and $2000\,\mathrm{m} \times 2000\,\mathrm{m}$ respectively. This means that when comparing one detector to the next-largest one, the string distance in both x- and y-direction doubles. A surface area comparison is depicted in Figure 12, while the three-dimensional view can be found in Figure 23.

For another, we can also compare the base square kilometer detector of 10×10 strings with ones with the same total number of strings and the same surface area, but aligned in different ratios, one being 2×50 string on $200\,\mathrm{m} \times 5000\,\mathrm{m}$ and one 5×20 strings on $500\,\mathrm{m} \times 2000\,\mathrm{m}$. Those three setups are shown in Figure 13 for a depiction of their surfaces and in Figure 24 for their three-dimensional models.

Those two comparisons allow us to draw conclusions on the effects of varying the string density while keeping the same square detector shape or conversely, changing the detector surface shape while the string density is being kept constant.

3.2.5 Application to Position Reconstruction

For the position reconstruction, the general way of reconstructing is the same as for the energy. Nevertheless, differences are apparent, with the most notable being that three variables for the three different space coordinates need to be reconstructed simultaneously while the true event energy is assumed to be known. This thesis does not include a reconstruction of both the energy and the position of an event at once. The Fisher Information for the position reconstruction hence becomes a matrix $M[3 \times 3]$ according to Equation 8 with matrix element consisting of the partial derivatives of the logarithmic likelihood curve with respect to variable i and j.

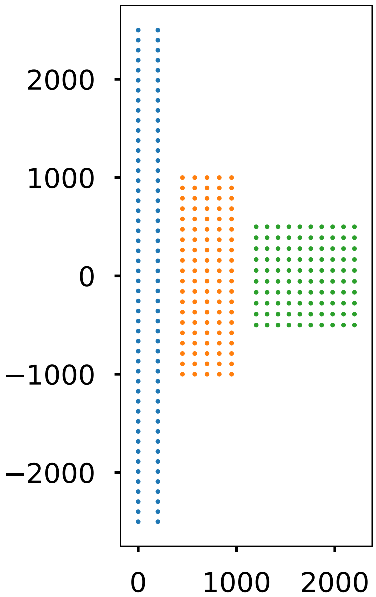

Figure 13: Surface Area Comparison of Three Rectangular Detectors of Different Side Length Ratios. To keep the string distance the same, the 100 strings in total were placed in the same aspect ratio as the detector side lengths. On the right, 10×10 strings cover an area of $1000\,\mathrm{m} \times 1000\,\mathrm{m}$. The configuration in the middle consists of 5×20 strings in an area of $500\,\mathrm{m} \times 2000\,\mathrm{m}$, effectively doubling one side and halving the other compared to the square detector. The setup on the left is equipped with 2×50 strings covering $200\,\mathrm{m} \times 5000\,\mathrm{m}$. Due to a mistake in the initialization of the module positions, the string distances are not equivalent for all three detectors, with the longest detector clearly displaying a larger distance in one dimension compared to the other dimension.

First, the derivative of the negative log-likehood amount to

$$\begin{aligned}
\frac{\partial}{\partial x_i}(-\ln L) &= \frac{\partial}{\partial x_i}\sum_{n=1}^{N}\Big(-k_n\ln\big(\mu(r,E)\big)+\ln(k_n!)+\mu(r,E)\Big)\\
&= \sum_{n=1}^{N}\left(\frac{-k_n}{\mu(r,E)}\frac{\partial\mu(r,E)}{\partial x_i}+\frac{\partial\mu(r,E)}{\partial x_i}\right)\\
&= \frac{\partial\mu(r,E)}{\partial x_i}\sum_{n=1}^{N}\left(\frac{-k_n}{\mu(r,E)}+1\right),
\end{aligned}$$

so that

$$\frac{\partial}{\partial x_i}(-\ln L) = \frac{\partial\mu(r,E)}{\partial x_i}\sum_{n=1}^{N}\left(\frac{-k_n}{\mu(r,E)}+1\right), \tag{14}$$

with the derivative of the photon yield with respect to a space coordinate denoted by

$$\frac{\partial\mu(r,E)}{\partial x_i} = -\mu(r,E)\cdot\left(\frac{1}{\lambda_p}+\frac{1}{r}+\frac{1}{\lambda_c\tanh(\frac{r}{\lambda_c})\cosh^2(\frac{r}{\lambda_c})}\right)\frac{x_i-x_{i,\mathrm{DOM}}}{r}. \tag{15}$$

The calculation of Equation 15 can be found in Section A.2.
Inserting Equation 14 and Equation 15 into Equation 8 yields

$$\begin{aligned}
\mathcal{F}_{ij} &= \mathbb{E}\left[\left(\frac{\partial}{\partial x_i}\ln L\right)\cdot\left(\frac{\partial}{\partial x_j}\ln L\right)\right]\\
&= \mathbb{E}\left[\left(\frac{\partial\mu(r,E)}{\partial x_i}\sum_{n=1}^{N}\Big(\frac{-k_n}{\mu(r,E)}+1\Big)\right)\cdot\left(\frac{\partial\mu(r,E)}{\partial x_j}\sum_{n=1}^{N}\Big(\frac{-k_n}{\mu(r,E)}+1\Big)\right)\right]\\
&= \mathbb{E}\Bigg[\left[\sum_{n=1}^{N}\Big(\frac{-k_n}{\mu(r,E)}+1\Big)\right]^2\frac{\mu(r,E)^2}{r^2}\cdot\left(\frac{1}{\lambda_p}+\frac{1}{r}+\frac{1}{\lambda_c\tanh(\frac{r}{\lambda_c})\cosh^2(\frac{r}{\lambda_c})}\right)^2\\
&\quad\cdot\big(x_i-x_{i,\mathrm{DOM}}\big)\big(x_j-x_{j,\mathrm{DOM}}\big)\Bigg],
\end{aligned}$$

hence

$$\begin{aligned}
\mathcal{F}_{ij} = \mathbb{E}\Bigg[&\left[\sum_{n=1}^{N}\Big(\frac{-k_n}{\mu(r,E)}+1\Big)\right]^2\frac{\mu(r,E)^2}{r^2}\cdot\left(\frac{1}{\lambda_p}+\frac{1}{r}+\frac{1}{\lambda_c\tanh(\frac{r}{\lambda_c})\cosh^2(\frac{r}{\lambda_c})}\right)^2\\
&\cdot\big(x_i-x_{i,\mathrm{DOM}}\big)\big(x_j-x_{j,\mathrm{DOM}}\big)\Bigg].
\end{aligned} \tag{16}$$

Similarly, Equation 10 can also be adapted for the position reconstruction. Inserting $\mu(r,E)$ from Equation 3 as λ and $x_{i,j}=\vartheta_{i,j}$ as well as Equation 15 for the derivative of the photon yield with respect to one dimension of the event position, we arrive at

$$
\begin{aligned}
\mathcal{F}_{ij} &= \frac{1}{\mu(r,E)} \cdot \frac{\partial \mu(r,E)}{\partial x_i} \cdot \frac{\partial \mu(r,E)}{\partial x_j} \\
&= \frac{1}{\mu(r,E)} \cdot \left(-\mu(r,E) \cdot \left(\frac{1}{\lambda_p} + \frac{1}{r} + \frac{1}{\lambda_c \tanh(\frac{r}{\lambda_c}) \cosh^2(\frac{r}{\lambda_c})} \right) \frac{x_i - x_{i,\mathrm{DOM}}}{r} \right) \\
&\quad \cdot \left(-\mu(r,E) \cdot \left(\frac{1}{\lambda_p} + \frac{1}{r} + \frac{1}{\lambda_c \tanh(\frac{r}{\lambda_c}) \cosh^2(\frac{r}{\lambda_c})} \right) \frac{x_j - x_{j,\mathrm{DOM}}}{r} \right) \\
&= \frac{\mu(r,E)}{r^2} \cdot \left(\frac{1}{\lambda_p} + \frac{1}{r} + \frac{1}{\lambda_c \tanh(\frac{r}{\lambda_c}) \cosh^2(\frac{r}{\lambda_c})} \right)^2 \cdot \big(x_i - x_{i,\mathrm{DOM}}\big)\big(x_j - x_{j,\mathrm{DOM}}\big),
\end{aligned}
$$

so that

$$
\mathcal{F}_{ij} = \frac{\mu(r,E)}{r^2} \cdot \left(\frac{1}{\lambda_p} + \frac{1}{r} + \frac{1}{\lambda_c \tanh(\frac{r}{\lambda_c}) \cosh^2(\frac{r}{\lambda_c})} \right)^2 \cdot \big(x_i - x_{i,\mathrm{DOM}}\big)\big(x_j - x_{j,\mathrm{DOM}}\big). \tag{17}
$$

After that, the optimization can be realized exactly as for the energy. For the uncertainty calculation via the Cramér-Rao bound, it is important to note that the uncertainty σ is now also a matrix of the same shape as the Fisher Information. So each entry of the σ matrix is calculated from the corresponding entry of the Fisher Information matrix according to Equation 7. The complete uncertainty σ then results from the diagonal entries of this matrix and amounts to

$$
\sigma_{tot} = \left(\sum_{i=1}^{3} \sigma_{ii}^2 \right)^{\frac{1}{2}}.
$$

3.3 Outlook to Muon Track Events

This section presents the implementation of the muon track event simulation and the basic energy reconstruction. Then follows a brief discussion on how further reconstruction aspects might be implemented in the future.

For the muon tracks, the simulation configuration is similar, with events initialized with random energies and positions. One difference is that now, in addition to the initial positions, we also need to implement the track direction. This is done by drawing spherical coordinates θ uniformly from $[0;\pi]$ and ϕ uniformly from $[0;2\pi]$. The resulting position after a conversion into cartesian coordinates denotes the event direction.

Another difference between the cascade and the muon track events lies in the way the photon yield arriving at the individual DOMs is implemented. For this, the muon track needs to be determined as a trajectory based on the initial position where the muon first appears and extending in the initialized direction of travel.

The photon yield depending on the event energy and the distance of the DOMs to the closest point of the muon track as provided by Aartsen et al. (2014), Rädel and Wiebusch (2012), and Abbasi et al. (2010) amounts to

$$
\mu(r,E) = l_0(E) \cdot A \frac{1}{2\pi \sin(\theta_c)} e^{-\frac{r}{\lambda_p}} \frac{1}{\sqrt{\lambda_\mu r} \tanh(\sqrt{\frac{r}{\lambda_\mu}})}, \tag{18}
$$

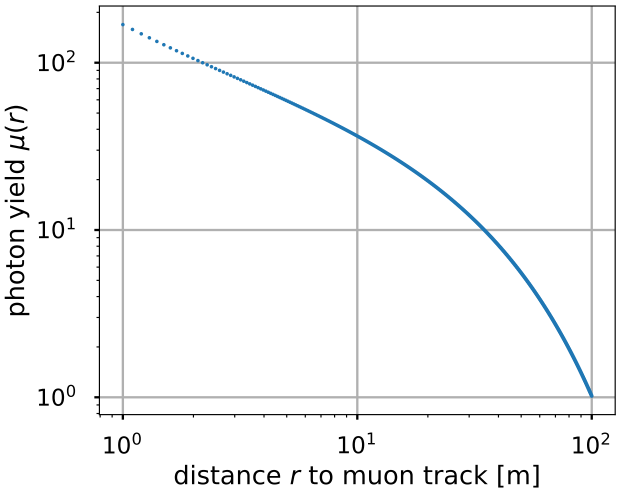

Figure 14: Measured Photon Yield of a Muon Track Event Depending on the Distance to the Track. This is an illustration of Equation 18 for an energy of $E = 10^3\,\mathrm{GeV}$. The photon yield first decreases linearly in a double-logarithmic plot. After about 30 m from the muon track, the slope increases continuously.

with

$$\begin{aligned}
\theta_c &= \arccos(\frac{1}{1.33}), \\
\lambda_c &= \frac{\lambda_{\text{scat}}}{3\zeta}, \\
\lambda_p &= \sqrt{\frac{\lambda_{\text{abs}}}{\lambda_{\text{scat}}}}, \\
\lambda_\mu &= \frac{\lambda_c}{\sin^2(\theta_c)} \frac{2}{\pi\lambda_p}, \\
\zeta &= e^{-\frac{\lambda_{\text{scat}}}{\lambda_{\text{abs}}}}, \\
\lambda_{\text{abs}} &= 125, \\
\lambda_{\text{scat}} &= 33, \\
A &= 84 \cdot 10^{-4}\text{m}^2.
\end{aligned}$$

It utilizes the Frank-Tamm formula as found in Lin and Scheihing-Hitschfeld (2026), originally formulated by Tamm and Frank (1967).
Figure 14 shows the photon yield resulting from this equation as a function of the distance to the muon track.
The energy reconstruction can be realized equivalently to that for cascade events. We can again determine the likeliest energy value as the one minimizing $-\ln L$. This similarity should also hold for the various means of calculating the uncertainty estimation of the energy reconstruction, though this is not implemented in the current simulation.
For muon tracks, the position reconstruction is also not implemented. It is more complicated compared to the cascade events, especially since here, the initial position of the event might lie far outside the detector and hence not be discernible. Instead, the

linear trajectory of the event is a more complete event description than where on this track the event was initialized as the latter does not include the event direction. This means that for an actual reconstruction, it is more interesting to reconstruct the track through the detector, which could be done for instance by converting positions into spherical coordinates and then setting the initial position of the event to a certain radial distance r from the center of the detector, which might coincide with the coordinate center. Then to reconstruct the track, only the two angles θ and ϕ as well as a closest distance between the track and the detector center need to be reconstructed.

4 Implementation

This section describes the details of the implementation for both the simulation and the reconstruction code.

4.1 Simulation

First, the implementation of the simulation of the detector and the events is presented.

4.1.1 Detector Geometry Setup

The simulation begins by initializing a detector consisting of `xnum`-, `ynum`-, and `znum`-many detection units in x-, y-, and z-direction, respectively. There, the DOMs are spread out over a distance $|\texttt{x\_max} - \texttt{x\_min}|$ and analogously for the y- and z-direction. For our specific implementation, the values are chosen such that the point $(0, 0, 0)$ is at the center of the detector, meaning that e.g. `x_min` and `x_max` are centered around 0 and likewise for the two other dimensions. Additionally, all three dimensions being set individually regarding the detector length and the number of DOMs facilitates arbitrary detector geometries.
To translate the input parameters into a usable array of DOMs, at first three arrays of the points in x-, y-, and z-direction are created by linearly arranging e.g. `xnum`-many points within the distance between `x_min` and `x_max`. Then these arrays are nested into one using for-loops; each array element containing the string number, the DOM number, and the x-, y-, and z-position.

4.1.2 Event Initialization

For the events, we can – as it was done for some experiments in this thesis as well – initialize them in a volume slightly larger than the detector itself, for instance with a border of 5% of a detector length on all 6 sides, which corresponds to a length for e.g. x of $1.1 \cdot |\texttt{x\_max} - \texttt{x\_min}|$. The three dimensions of the event positions are then all drawn uniformly between their minimal and maximal possible values.
Alternatively, we can also initialize events in a fixed event volume significantly larger than the detector. This method has the advantage of being able to more easily compare for example an effective volume. Here, one sets a cuboid volume centered on the detector center, with side lengths greatly exceeding the expected detector size. Then all three components of the position are each drawn uniformly from their respective event volume length.
In addition to the position, the events also need to be initialized with a certain energy deposited at its position. There, usually the decimal power is drawn uniformly from the interval $[2; 6]$ so that the energies are spread logarithmically within $[10^2\,\text{GeV}; 10^6\,\text{GeV}]$. But apart from that, the energies of all events can also be assigned specific values from the start by initializing them in an array.

4.1.3 Geometry Calculations

To calculate the effective detection volume as described by Equation 1, we first need to determine both the detector volume and the volume spanned by the events.

The detector volume is generally easy to calculate with a cuboid-shaped initialization such as described above. Still, to keep this part of the code as general as possible, the volume is determined using the volume of the convex hull spanned by all detection modules. A convex hull is the shape created by connecting all outermost points of a body with lines and can thus be used as a universal method to calculate the outer hull of any collection of points in a three-dimensional space.
The actual volume of events can be calculated similarly, using again the convex hull to infer the shape spanned by all event points. But since we investigate how a detector's effective volume might change depending on the energy of events, the event volume is to be determined individually per each event energy. This can be realized by initializing several energies and for each energy, placing many events at different positions within the initialized event volume. This means that the effective volume will only be calculated for the specific predetermined energies instead of for all possible energies that might also be randomly drawn from the interval described above. In the future, a broader implementation might hence be interesting, where the event energies are binned and the effective volume is calculated for each bin. The method for calculating an effective volume is presented in Equation 1.
Apart from knowing the event and DOM positions and their volumes, it might also be interesting to directly compare values for the x-, y-, and z-lengths of different detectors, their distances between strings and between DOMs within a single string, as well as the surface area. Hence, these are all printed in an output file created individually for each detector geometry. It should be noted that for the surface area, currently a rectangular area is assumed as all heretofore simulations were run for cuboid detectors only.

4.1.4 Measurement Samples

For the actual measurements of photon numbers arriving at the DOMs, the so-called photon yield needs to be calculated for each DOM using the DOM positions and the energies and positions of events. For this, we use Equation 3 for cascade events and Equation 18 for muon track events. With the use of arrays, the photon yield for all events at all DOMs can be quickly determined once the distances between DOMs and events are known. The distances can be determined as the norm of the difference between a DOM position and the event position.
To increase statistics and imitate the measurement of several events with similar initial positions and energies, we then randomly draw several samples of the previously determined true photon yield, which is taken as the expectation, from a Poisson distribution. When the inputs are compared to the parameters in Equation 4, the expectation amounts to the calculated true photon yield, so $\lambda = \mu(r, E)$, and the sampled photon numbers drawn are denoted by k.

4.1.5 Event Acceptance

In the following, a detection threshold for events is applied to the Poisson-distributed samples so that only those events are accepted for which a certain minimal number of photons are measured in all DOMs in total. This filters out events outside a proper detection range. To be precise, the events with sampled measurements at least as large as a predetermined `event_acceptance_threshold` $= 5$ are masked, for instance their

photon yields, the energies or the event positions. All events below this threshold have their corresponding sampled photon yield array entries ignored.
The effective volume can then be calculated using the detected number of events, which can in turn be derived with the help of the above-mentioned mask.
In the future, one could extent this acceptance threshold so that events also need to be detected in a certain number of DOMs or even a certain number of strings, which would ensure that only events with a considerable visibility remain.

4.2 Reconstruction

Now the implementation of the reconstruction methods are examined in detail.

4.2.1 Likelihood Minimization

For minimizing a likelihood curve, it is first necessary to implement a functioning likelihood calculation. The likelihood follows Equation 5, where a singular likelihood function L_i, so for one DOM, is dependent on the calculated true photon yield $\mu(r, E) = \lambda$ and the randomly drawn photon measurement k_i. As we are actually interested in the negative logarithm of the total likelihood $-\ln L$, this equation turns into Equation 6, which depends on the same parameters as the aforementioned likelihood functions L_i per DOM.
The following likelihood minimization has the goal of determining the best fit value for either the event energy E or the distance r between the event and the DOM positions. To attain this goal, the main steps are

1. Implementing the formula for Equation 6

2. Creating a grid of possible values for the parameter we want to optimize

3. Wrapping the log-likelihood function so that it only depends on said parameter

4. Inserting the grid into the wrapper function to receive a result for the log-likelihood scan of each possible parameter value. As the likelihood, and by extension also its logarithm, is a measure of how likely a result is, the grid value with the largest likelihood – and thus smallest negative log-likelihood – is expected to be the one closest to the true parameter value.

5. Minimizing the spline fit of the function instead of merely looking for the smallest point in a grid to determine the true minimal value

All of these steps will be discussed in detail in the following.
Since the energy reconstruction encompasses the optimization of a single parameter, it is easier than the simultaneous reconstruction of the three-dimensional event position. Hence, the former was implemented first and will consequently also be explained first in this section.
To determine $\mu(r, E)$ as it appears in the log-likelihood function, we first needs to calculate the distances r between the initialized event positions and the DOMs. Then, the photon yield `mu_return` can be calculated from this distance and the energy input parameter of the log-likelihood function. Due to not every DOM detecting photons for every event, various entries of the resulting array will be 0, and because of numerical

errors, some might even be negative. To account for the logarithm of those entries not being defined, even though its calculation is needed for Equation 6, entries with values ≤ 0 are set to a small but positive value of 10^{-100} with its logarithm being a large negative value as $\ln x \to -\infty$ for $x \to +0$. Then the individual $-\ln L_i$ can be determined with the use of the aforementioned equation, where the logarithm $\ln(k_i!)$ of the measured photon number is calculated via the equivalent gamma function $\Gamma(k_i+1)$ of the sampled photon measurement values with the addition of 1 each. Afterwards, the L_i for all DOMs can be summed up to receive a total $-\ln L$ for each measurement sample of one event.

A wrapping function is then created which depends only on the energy E and returns the previously described calculation of the total negative log-likelihood. This is viable since all other parameter inputs of said log-likelihood are values that, at least at this point of the, are already fixed and can thus be treated like constants within this wrapper. Next up, a grid of some possible energy values within the investigated range of [10^2 GeV; 10^6 GeV] is established with `gridsize`-many points spread logarithmically between those edge values. Those points are then expanded to the necessary array shape by filling the added dimension with those same values.

Then, a so-called likelihood scan is realized by iteratively calculating the log-likelihood for each point in the energy grid while the event positions are the ones we initialized and hence we assume them to be known. This likelihood scan serves as one of several inputs for a larger function that reconstructs the most likely energy value and calculates the $\pm 1\sigma$ interval as explained in Section 3.2.2. For each event and there, for each measurement sample, we inspect the minimal value of the likelihood scan array and takes the corresponding energy grid entry as an initial guess for the minimal energy, also called `x_min_guess`. To find the optimal parameter value and corresponding function value where the negative log-likelihood is minimal, we first have to define the function we want to minimize. Here, this is the wrapping function that creates a log-likelihood function calculation depending only on the energy. This function is then optimized with regard to the energy using the L-BFGS-B algorithm, an extension of the Broyder-Fletcher-Goldfarb-Shanno algorithm (BFGS) (Fletcher, 1987) adapted for limited memory ("L-" prefix) extended for bound constraints ("-B" suffix) (Byrd et al., 1995).

One noteworthy detail of this optimization is that the function input is actually $10^{\log_{10}(E)}$ with the guess also translated to $\log_{10}$(`x_min_guess`). This is done for improved numerical stability. The resulting optimization output is the estimated parameter value `x_opt` where the function is minimal and a corresponding function value `f_opt` for this minimal point. Due to the nature of the adjusted function input, `x_opt` is not the actual value where the negative log-likelihood Equation 6 is minimal, as that is $\texttt{x\_min} = 10^{\texttt{x\_opt}}$ instead. Still, the function value itself remains the same, hence $\texttt{f\_min} = \texttt{f\_opt}$.

Then, to determine the $\pm 1\sigma$ interval, a second function is defined using another wrapping function which is the same as the previous one except for shifting the negative log-likelihood downwards by its function minimum and a factor of 0.5, resulting in $-\ln L - y_{min} - 0.5$, so that the roots are exactly the points $x_{min} \pm 1\sigma$ around the parameter value of the function minimum as described in Section 3.2.2. We can then determine the roots of this shifted function with the help of Brent's root-finding method (Brent, 1973) which needs to be provided with an interval that contains the wanted root. As the minimum of the shifted function is certainly below 0 by design, its parameter value x_min is taken as the right end of the bracketing interval for the left root and as the left end of the interval for the right root. The left end of the interval for the left root is simply the first array element of the energy grid, and similarly, the right end of the interval for the right root is the last entry of the energy grid array. The 1σ width is then half the distance between the left and right root. When the event energy is sufficiently close to the minimally or maximally possible energy of the interval $[10^2\ \mathrm{GeV}; 10^6\ \mathrm{GeV}]$, there might not exist a left or right root of the shifted log-likelihood curve within the observed interval. To keep the calculation from failing in these edge cases, the according left or right root is set to an invalid value whenever the shifted function of either the very first or the last energy grid value is negative. This does not affect any resulting calculations other than that in this instance, the calculated 1σ width is then also an invalid value.

For the position reconstruction, the log-likelihood minimization and hence finding the optimal position works similarly. Still, some differences are apparent as now, three parameters for the three dimensions of the event position are optimized simultaneously. First, the initial calculation of the sum of individual negative log-likelihoods according to Equation 6 remains the same as described for the energy. But then the wrapping function needs to make the log-likelihood solely dependent on the event positions. Additionally, the position grid needs to be created differently as well. Here, the current implementation allows for two options. One is that the events are all initialized within a fixed volume that is the detector volume with an additional 5% side length border on all sides. The other allows for a larger event initialization volume significantly larger than the detector. For the first version, the possible x-positions are determined as gridsize_x-many points spread linearly within the distance $|1.1 \cdot \texttt{x\_max} - 1.1 \cdot \texttt{x\_min}|$. The positions in the y- and z-direction are created analogously. The second method creates the same points instead within symmetrical distance, with for instance the points in the x-dimension spread linearly between -x_event_pos and +x_event_pos, corresponding to the minimal and maximal extension of the event volume. The other dimension are again implemented analogously. With both methods, for each of the three dimensions, the number of points can be chosen individually, which might be useful for detectors with different detection module densities in the three dimensions.

From those three one-dimensional arrays, we then want to create a grid of points that does not merely create one point from the first entry of of all three arrays etc., but instead we want a grid where for every entry in the first grid, we then iterate over every entry in the second and within that, also over every entry in the third grid so that for a single x- and y-coordinate, we can still find combinations with the whole array of different z-coordinates that together are then a single string. To realize this goal, we first create three three-dimensional arrays of shape (gridsize_x, gridsize_y, gridsize_z) named x_grid, y_grid, and z_grid where each one contains all values of the corresponding one-dimensional array with the values in x_grid ordered along the 0-axis and each value repeated along the first and second one. Similarly, the y_grid values are ordered along the first axis and repeated along the others, while z_grid has its values aligned along the second axis. This means that we have three grids with the same shapes but different values that are repeated at different intervals, with , e.g., every value of x_grid appearing $\texttt{gridsize\_y} \cdot \texttt{gridsize\_z}$-many times.

Then, the full grid of possible positions is built by first flattening all three of those grid

arrays so that what remains are three one-dimensional arrays containing the values of the linearly spread points of the x-, y-, and z-dimension, respectively, each with a different permutation of repeated sequences. Afterwards, we column-stack these flattened version of the grid arrays, which means that we iteratively go through all three flattened arrays and each time take the i-th entry of all three arrays, combining them into a new array element $[x_i,\ y_i,\ z_i]$. This resulting grid of event positions then has the shape $(\texttt{gridsize\_x} \cdot \texttt{gridsize\_y} \cdot \texttt{gridsize\_z}, 3)$ as expected and contains all possible combinations of coordinates from the initial linear spreads for all three dimensions.
The following is an exemplary depiction of the process detailed just now. The array entries $1, 2, 3, A, B, C, D, \alpha, \beta$ are arbitrary values used for illustration and to easily distinguish between the contents of the different arrays.

$$
\begin{gathered}
x = [1, 2, 3], \quad y = [A, B, C, D], \quad z = [\alpha, \beta], \\
x_{grid}, y_{grid}, z_{grid} = \text{np.meshgrid(x, y, z, indexing = "ij")}, \\
x_{grid} = \begin{bmatrix} \begin{bmatrix} [1, & 1], \\ [1, & 1], \\ [1, & 1], \\ [1, & 1] \end{bmatrix}, & \begin{bmatrix} [2, & 2], \\ [2, & 2], \\ [2, & 2], \\ [2, & 2] \end{bmatrix}, & \begin{bmatrix} [3, & 3], \\ [3, & 3], \\ [3, & 3], \\ [3, & 3] \end{bmatrix} \end{bmatrix}, \\
y_{grid} = \begin{bmatrix} \begin{bmatrix} [A, & A], \\ [B, & B], \\ [C, & C], \\ [D, & D] \end{bmatrix}, & \begin{bmatrix} [A, & A], \\ [B, & B], \\ [C, & C], \\ [D, & D] \end{bmatrix}, & \begin{bmatrix} [A, & A], \\ [B, & B], \\ [C, & C], \\ [D, & D] \end{bmatrix} \end{bmatrix}, \\
z_{grid} = \begin{bmatrix} \begin{bmatrix} [\alpha, & \beta], \\ [\alpha, & \beta], \\ [\alpha, & \beta], \\ [\alpha, & \beta] \end{bmatrix}, & \begin{bmatrix} [\alpha, & \beta], \\ [\alpha, & \beta], \\ [\alpha, & \beta], \\ [\alpha, & \beta] \end{bmatrix}, & \begin{bmatrix} [\alpha, & \beta], \\ [\alpha, & \beta], \\ [\alpha, & \beta], \\ [\alpha, & \beta] \end{bmatrix} \end{bmatrix}, \\
x_{grid}.flatten() = \big[1, 1, 1, 1, 1, 1, 1, 1, 2, 2, 2, 2, 2, 2, 2, 2, 3, 3, 3, 3, 3, 3, 3, 3\big] \\
y_{grid}.flatten() = \big[A, A, B, B, C, C, D, D, A, A, B, B, C, C, D, D, A, A, B, B, C, C, D, D\big] \\
z_{grid}.flatten() = \big[\alpha, \beta, \alpha, \beta, \alpha, \beta, \alpha, \beta, \alpha, \beta, \alpha, \beta, \alpha, \beta, \alpha, \beta, \alpha, \beta, \alpha, \beta, \alpha, \beta, \alpha, \beta\big] \\
full\_grid = np.c\_[x_{grid}.flatten(), y_{grid}.flatten(), z_{grid}.flatten()] \\
full\_grid = \begin{bmatrix} [1, & A, & \alpha], \\ [1, & A, & \beta], \\ [1, & B, & \alpha], \\ [1, & B, & \beta], \\ [1, & C, & \alpha], \\ & \vdots & \end{bmatrix}
\end{gathered}
$$

The likelihood scan calculating the negative log-likelihood for each point in the position grid is determined similarly to the energy except that here, the inputs are the initialized energy values and the points in the position grid. Again, the individual log-likelihoods are then summed over the DOMs so that we once more receive the full negative log-likelihood $-\ln L = \left(\sum_{i=1}^{n} -\ln L_i\right)$ from Equation 6 for a drawn sample of a detected event for each of the $\texttt{gridsize\_x} \cdot \texttt{gridsize\_y} \cdot \texttt{gridsize\_z}$-many points within the whole position grid.

For the calculation of the most likely event position when considering the detected photon yields, we take the position grid point with the smallest resulting negative log-likelihood as an initial guess `x_min_guess`. Then, we define the function to be minimized as the wrapping function making the negative log-likelihood solely dependent on the event position.
Thereafter, we again optimize this function with the L-BFGS-B algorithm to receive the position `x_opt` and the corresponding likelihood value `f_opt` where the log-likelihood has its minimum. As the position points considered here are spread linearly instead of logarithmically as is the case for the energy, the optimization already works well when the position and its guess are inserted into the function directly without the power and logarithm discussed for the energy optimization. Hence, the optimal values from the return of the optimization are already those minimizing the negative log-likelihood, so `x_min` = `x_opt` and `f_min` = `f_opt`.

4.2.2 Uncertainty Estimation

As already mentioned in Section 3.2.2, there are multiple methods to determine the uncertainty of the reconstruction. First off, there is the general formula for calculating the Fisher Information as established in Equation 9 and Equation 8 for the one-dimensional and multi-dimensional case, respectively. Applied to the energy reconstruction, it results in Equation 12 which can be implemented easily with k_i being the sampled photon number detected at the i-th DOM, while $\mu(r, E)$ is provided by Equation 3. The results for the individual DOMs are then summed up and afterwards, we need to square this result. To calculate the expectation value, we then determine the mean of the equation result for the different photon yield samples drawn from the Poisson distribution.
Determining the derivative of the log-likelihood $\ln L$ with respect to the energy E can be done manually as shown when Equation 12 was derived. We verified that this is equivalent to the automated determination of gradient of the log-likelihood function of Equation 6, as implemented for instance in jax. Then, we square up the result and take its mean over the the measurement samples.
Determining the uncertainty on the position reconstruction can be realized similarly. The main difference here is that we use Equation 16 instead.
Alternatively, we can also calculate the Fisher Information by utilizing the simplified formula as seen in Equation 11 for the one-dimensional and Equation 10 for the multi-dimensional case. The application to the energy or position reconstruction works similar to what is described above for the other method. The main difference is the use of different equations, i.e. Equation 13 and Equation 17, respectively. This also means that we do not insert any drawn measurement samples. Hence, no mean needs to be determined. The equation results for all DOMs merely need to be summed up.
Whenever there is more than one measurement sample for an event, for the likelihood width method the mean of those several results is calculated. This allows us to compare this single resulting value per event with the other methods detailed above that also result in only one value per event.

5 Results

This section presents a detailed analysis of the results of the event reconstruction discussed in Section 3.2 for both the energy and the position of cascade-like event topologies. In addition, an outlook on the application of these reconstructions to track-like events is discussed at the end of the chapter.

5.1 Cascade Events

The first objective of this work is the analysis of cascade-type events and results on the possible reconstruction precision for both energy and interaction vertex position. This section summarizes the results of this investigation and compares the achieved performance of multiple detector configurations regarding the energy reconstruction.

5.1.1 Comparison of Energy Uncertainty Estimation Methods

We can compare the three different methods of calculating the uncertainty of the energy reconstruction. For one, we calculate the 1σ interval of the log-likelihood curves and for another, we use the two different equations for the Fisher Information as provided in Equation 12 and Equation 13. Together with the Cramér-Rao bound of Equation 7, the latter two result in two more values for the uncertainty estimation σ.
Applying all estimation techniques for the standard deviation, similar results are found. This is shown explicitly in Figure 15 for the energy reconstruction of six different cascade events. The coinciding results can be explained by the fact that the Fisher Information via Equation 12 is calculated as the expectation value, which corresponds to the mean value of the results from the different Poisson-distributed measurement samples of the photon yield at each DOM. Meanwhile, the Fisher Information as resulting from Equation 13 utilizes the known true value of the photon yield arriving at each DOM. This means that according to the law of large numbers as presented by Poisson (1837), with increased data sample statistics the sample mean will converge to the true mean of the Poisson distribution from which the samples are drawn. Additionally, the 1σ width resulting from the log-likelihood curve is also coinciding well with both results calculated with the Fisher Information, though most notably with the one from Equation 13 assuming a Poisson distribution and its known mean. The reason for this expected behavior is that this third result is based on estimating the uncertainty via the likelihood curves, which is an alternative to the calculation using the Fisher Information. Due to this close correspondence between the results and to keep the sample number sufficiently small for improved code performance, for the following experiments we use a sample number of 5 and examine only the uncertainty as resulting from Equation 13 unless stated otherwise.
It should be noted that the 1σ interval definition using the log-likelihood curve requires the approximated parabola to reach values of $\min(-\ln L) + \frac{1}{2}$ within the considered energy range. This means that for fits for which the log-likelihood curve runs out of the physical bounds of the system, no standard deviation can be estimated. To mitigate this problem, we increased the range of possible values spanned by the energy grid and thus also the range for the log-likelihood fit while not changing the range for the initialized parameter values, creating a wider log-likelihood fit encompassing the 1σ interval for more events.

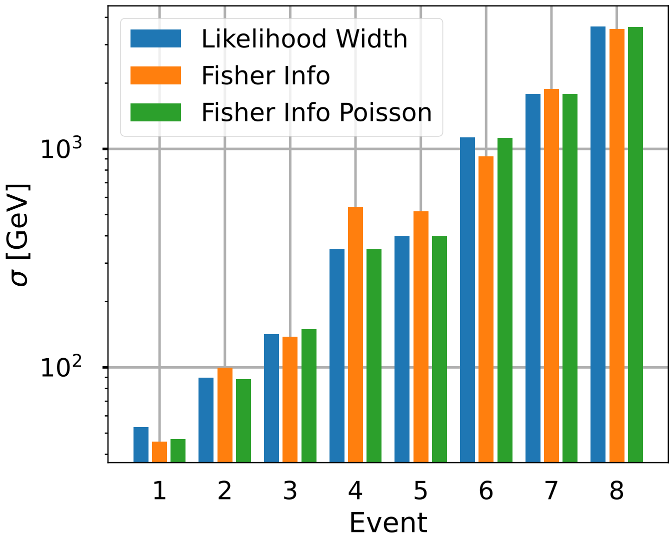

Figure 15: Histogram Comparing Different Methods of Calculating the Energy Uncertainty Estimation for Several Cascade Events. For each of the eight events, 10 samples are drawn from a Poisson distribution. The 1σ uncertainty is then calculated using the log-likelihood curve width, Equation 12, and Equation 13 as described in Section 3.2.2. The figure shows a notable agreement of all three results for each event, though most apparent between the first and the third method.

5.1.2 Energy Reconstruction Quality

To quantify the energy reconstruction results, we can compare the values of the true energy input of the simulation to the reconstructed energy values as presented in Figure 16 for one measurement sample per event.

It demonstrates that, especially when also considering the uncertainty as resulting from the 1σ interval of the log-likelihood curve, all points show a very good agreement of the simulated energies with the reconstructed ones. This is true for most measurements of events when initialized within the detector volume. One caveat though is that low-energy events that release comparatively few photons can lead to deviations of the reconstructed energy and higher uncertainties on said reconstructions. This could be because when the photon yield arriving at the DOMs is sampled from a Poisson distribution, already very low true photon yields will result in a relatively larger variation of this number of detected photons. Specifically, the number of DOMs detecting the event can then also fluctuate more as any module, depending on the measurement sample, might detect, e.g., either 0, 1, or 2 photons. As this applies to all detection units above a certain distance to the initial event position, this phenomenon has a significant impact on the reconstruction quality. Hence, it is more likely that the reconstructed energy strays farther from the true value for low energies. However, as the uncertainties are also larger in this case, the reconstructed energy would usually still be in agreement with the true energy within the 1σ interval.

Furthermore, we investigate the dependence of the relative uncertainty $\frac{\sigma}{E_{true}}$ on the true energy as shown in Figure 17a. The relative uncertainty is a measurement that

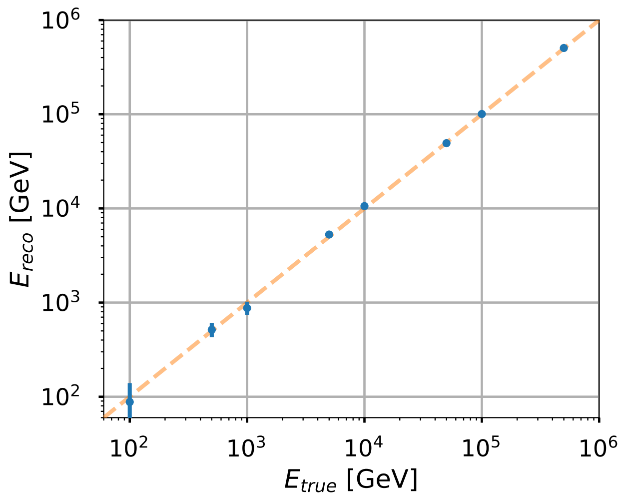

Figure 16: Comparison of the Reconstructed Energy and the True Energy. The error bars on the reconstructed energy correspond to the asymmetrical distances between the reconstructed energy values and the log-likelihood curve widths. All eight event reconstructions were realized for a single sample each for the sake of a cleaner illustration. The dashed line shows the identity, i.e. where the reconstructed energy and the true energy are equivalent. The figure shows that event though the statistics are low, the depicted reconstructed event energies correspond well to the true values within their 1σ intervals.

accounts for the fact that higher event energies will result in larger absolute uncertainty values. Generally, it is expected that said relative uncertainty decreases for higher energies. As already seen in Figure 16, at low energies, there can be some deviation of the reconstruction from the true energy value and the absolute uncertainties are also more pronounced. For those low-energy events, the statistical variation of already low photon numbers may make it harder to correctly identify the event energy. And on the other end of the spectrum, for high-energy events, we anticipate that statistics cause a relatively smaller variation in photon number. Additionally, we expect that the generally higher-energy photons released can consequently result in those photons arriving at more DOMs by traveling for farther distances. Both these effects improve the reconstruction quality at higher energies. Hence, we expect the relative uncertainty to decrease for higher energies, which is confirmed by Figure 17a.
From this figure specifically results that the relation between relative uncertainty and true energy is an approximately linear correspondence in a double-logarithmic plot. This means that it could be expressed using a power law $f(x) = ax^b$ as applying the logarithm to $f(x)$ yields

$$\log f(x) = \log(ax^b) = \log a + b \log x. \tag{19}$$

Hence, in a plot of $\log f(x)$ over $\log x$, b would correspond to the slope and $\log a$ to the offset.
Additionally, the relative uncertainty $\frac{\sigma}{E_{true}}$ can also be compared to the total number of photons measured at the DOMs, as depicted in Figure 17b. To be precise, it shows

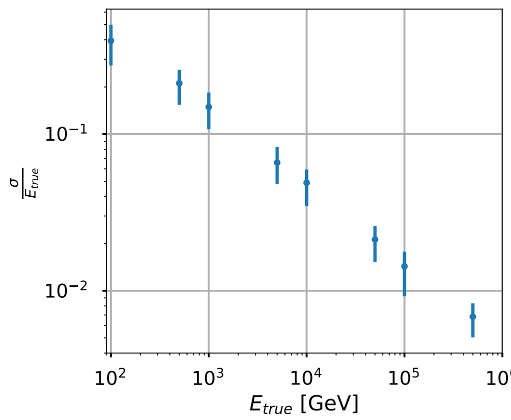

(a) Relative Uncertainty Depending on the True Event Energy.

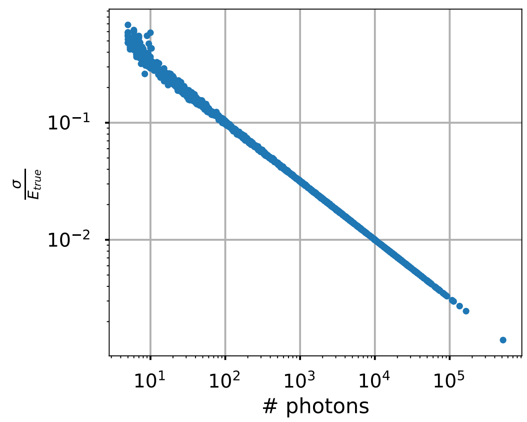

(b) Relative Uncertainty Over Number of Detected Photons.

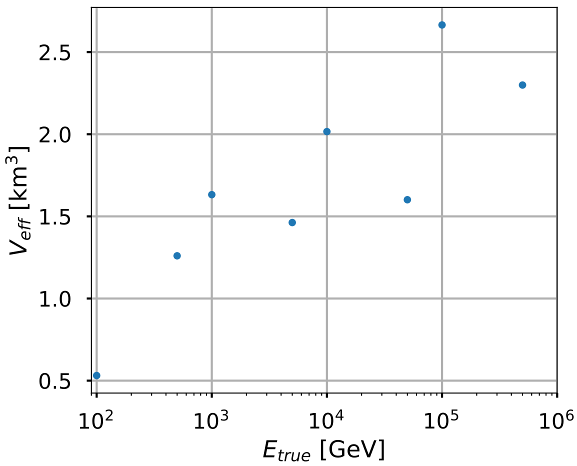

(c) Effective Volume per True Energy.

Figure 17: Three Experiments Investigating the Relative Uncertainty and the Effective Volume at Different Energies. All three experiments use the same eight event energies. Figure 17a and Figure 17b initialized 200 events for each energy, with their positions randomly drawn from the detector volume and the surrounding border. Then 5 samples of the total measured photon yield are drawn from a Poisson distribution. The relative uncertainty in Figure 17a denotes the median uncertainty of all event position for each energy, while the error bars correspond to the 18th to 84th percentiles. The photon number as depicted in Figure 17b denotes the sample mean for each event. For Figure 17c, for each energy, 1500 event positions are initialized within a fixed interaction volume. This volume is of a height of 3 km and a square surface area of 6 km by 6 km, centered on the detector center, resulting in a total volume of 108 km^3. Again, the photon yield is drawn with a sample number of 5. The relative uncertainty decreases linearly in the double-logarithmic plots for both increasing true energy and increasing photon numbers according to Figure 17a and Figure 17b. Meanwhile, the effective volume increases for larger event energies up to approximately 2.5 km^3.

the relative uncertainty over the sample mean of the total photon number for all event positions at each energy as individual points on a double-logarithmic plot. We can find a similar relation of the uncertainty to the total number of photons as before, namely also that of a power law. This is expected since the the true number of photons arriving at the DOMs is directly proportional to the energy deposited by an event as provided by the model description in Equation 3. Specifically, we can take a second power law $g(z) = u \cdot z^w$, and utilizing the linear proportionality $z = cx$ and that both plots show the relative uncertainty, so $f(x) = g(z) = g(cx)$, we can compare $\log g(cx)$ to Equation 19 to arrive at

$$\begin{aligned}
\log a + b \log x &= \log u + w \log(cx), \\
\log a + b \log x &= \log u + w \log c + w \log x, \\
\log a + b \log x &= \log(u \cdot c^w) + w \log x.
\end{aligned}$$

Hence, expressing the second power law in terms of the constants of the first one with $w = b$ and $u = \frac{a}{c^b}$ results in

$$\begin{aligned}
f(cx) &= \frac{a}{c^b}(cx)^b, \\
\log f(cx) &= \log\left(\frac{a}{c^b}\right) + b \log(cx).
\end{aligned}$$

This means that when plotting $\log f(cx)$ over $\log(cx)$, the new offset is $\log\left(\frac{a}{c^b}\right)$, while the slope is identical to that in Figure 17a. Visually, this also appears to be the case as the linear curve's slope in both figures is approximately $-\frac{1}{2}$.
It should be noted that the relative uncertainty over the mean photon number expresses different properties than when plotted over the true energy. For instance, we cannot compare the vertical spread in uncertainty per photon number in Figure 17b to the spread per true energy expressed as error bars in Figure 17a. Instead, for each set of events of the same energy displayed as a vertical array in Figure 17a the different event positions vary significantly in their distance to the closest detector module. This means that despite the same amount of energy released for all events of the same energy, the number of photons arriving at the DOMs differ noticeably. When considering the absolute uncertainty over photon number, then each energy set has the same slope, but a different offset, with higher energies corresponding to larger offsets. Additionally, the diagonal spread for higher energies is visibly larger. The offset then coincides once the uncertainty is divided by the true energy. This behavior is in agreement with our expectation that low-energy events outside the detector are mostly filtered out by our detection threshold, while many more high-energy events pass this threshold even when also initialized outside the detector. Hence, a high-energy event with a large distance to the detector, with the initial position known by design of the reconstruction, may result in approximately the same mean amount of total detected photons as a low-energy event within the detector. Those two events then have significantly different absolute uncertainties in their energy reconstruction when their positions are known because higher energies also result in larger absolute values for the uncertainties and vice versa. This is then also the reason why when the relative uncertainty is examined as shown in Figure 17b, all results lie on a single line.
The spread in the upper left corner of Figure 17b, so for few photons or a large relative uncertainty, is due to the very low mean photon number. Specifically, the mean values

of the Poisson-distributed photon yield samples do not necessarily correspond well to the uncertainties displayed, as the latter is calculated using the true photon number according to Equation 13. So investigating this relative uncertainty in relation to the mean photon number is merely done to include some semblance of statistical variation that is not inherently present in the relative uncertainty. Nevertheless, this comparison shows a trend of some deviation at low photon numbers from the straight line. The reason for this is the detection threshold, which results in a cutoff of all samples with a total photon number < 5. So when the true photon number as calculated in Equation 3 is very small, possibly even below this threshold, it can lead to cases where some measurement samples are filtered out and others remain, depending on the drawn sample value. Consequently, the mean of the remaining photon numbers is then by design ≥ 5 and does not coincide with the true photon value. This means some points of relative uncertainty will be shifted towards larger photon numbers compared to where they whould truly lie.

5.1.3 Effective Detection Volume

After quantifying the performance for the energy reconstruction of cascades, the next step is to investigate how the effective detection volume depends on the event energy. Calculating the effective volume using Equation 1 provides a mean of quantifying the volume of events a detector can actually observe. It can be calculated as a single effective volume or for individual energy values so that an energy-dependent effective volume can be studied. In the future, this effective volume could even be determined for binned energies so that our results for discrete energy values could be confirmed for an extension to continuous inputs.
Figure 17c depicts the effective volume for several energies, each with 200 different event positions initialized within a constant interaction volume significantly larger than the detector volume. It shows a trend of the effective volume increasing for events of larger energies. This correspond well to our expectation that a lower event energy results in the released photons traveling a shorter distance before being scattered and absorbed and hence a lower probability of passing our detection threshold. Additionally, cascade events in our simulation are implemented so that the photons are released homogeneously in the complete solid angle. Thus, for events initialized outside the detector volume, a smaller fraction of photons can possibly reach any sensor module compared to events fully contained in the detector. This fraction decreases further with a larger distance of the event to the nearest DOM. Hence, events positioned outside the detector need a significantly larger energy to pass the detection threshold. Still, in the figure we can also observe deviations from this general behavior. A possible explanation could be that 200 positions per event energy do not lead to large enough statistics considering the large interaction volume as well as our trigger condition. In the future, the experiment could hence be repeated with an increased position number per energy.

5.1.4 Comparison of Different Detector Configurations

After conducting these extensive experiments for our cubic base detector, the next step is to investigate how the detector configuration influences the reconstruction quality, its uncertainty, and the effective volume.

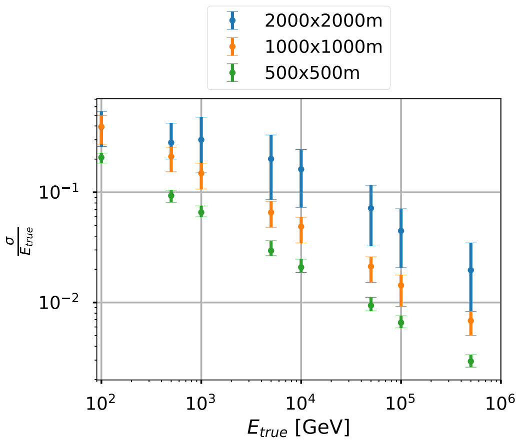

(a) Relative Uncertainty Depending on the True Event Energy for Three Detectors with Square Surfaces.

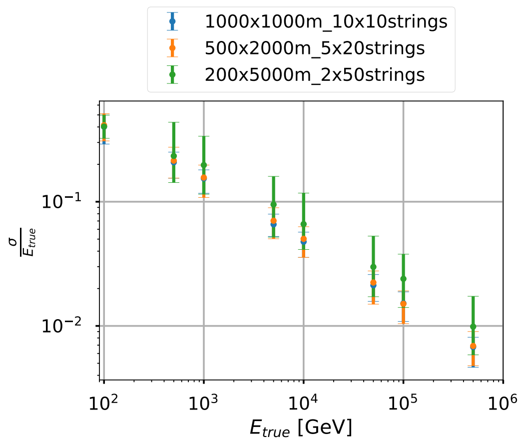

(b) Relative Uncertainty per True Event Energy for Three Rectangular Detectors of Different Side Length Ratios.

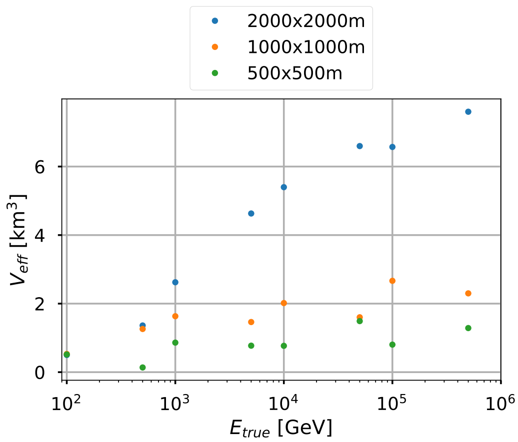

(c) Effective Volume Depending on the True Energy for Three Detectors with Square Surfaces.

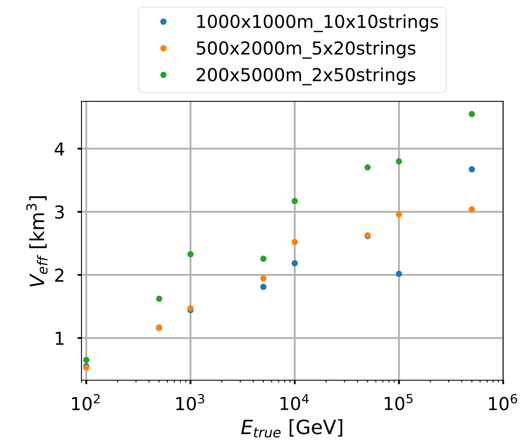

(d) Effective Volume per True Energy for Three Rectangular Detectors of Different Side Length Ratios.

Figure 18: Four Experiments Investigating the Relative Uncertainty and the Effective Volume at Different Energies for Two Sets of Detector Configurations. The setup for all plots is the same as for the corresponding figure in Figure 17. When examining the first detector set, Figure 18a shows that the relative uncertainty increases for all energies with a larger detection volume, constant string number, and hence a lower DOM density. Additionally, the spread denoted by the error bars also increases with a lower module density. For the effective volume as displayed in Figure 18c, we can observe that a larger detector with lower string density results in a larger effective detection volume for all energies of at least 10^3 GeV. The distinction is most significant for large energies and between the largest detector and the medium-sized one. For the second set of detectors, the results are not as significant. The detector of 2 by 50 strings shows both a larger relative uncertainty in Figure 18b and a larger effective volume in Figure 18d while the other two configurations are barely distinguishable.

For this, one experiment was to compare three differently-sized detectors with square surfaces as described in Section 3.2.4 and presented in Figure 12 and Figure 23.

The relative uncertainty on the energy reconstruction of those detectors for different event energies is presented in Figure 18a. We can again identify all the behaviors discussed for the cubic kilometer detector in Figure 17a. Additionally, it is apparent that the relative uncertainty increases with a larger detection area and hence a lower string density. The only exception is at the smallest energy of 100 GeV, where the largest detector seems to result in approximately the same relative uncertainty as that of the medium-sized detector, though the smallest detector still results in the smallest uncertainty.

For one, the general behavior is expected because when the string density is lowered, the maximal possible distance between a DOM and an event within the detector increases. This means that even though the event position is known by design, for an event of the same energy, the energy reconstruction will be less precise for a detector with lower string density as comparatively less photons reach a detection module. For another, this exception to the rule for the smallest energy could be due to small-energy events only releasing a small number of low-energy photons that can only cover a smaller distance before being absorbed. Hence, the "visible volume" around a DOM is accordingly small for small energies. Thus in this case, all detectors appear approximately equally "sparse" and the relative uncertainty is similar for any low-energy cascade event.

Additionally, the spread of the relative uncertainty distributions is also significantly larger for larger detector areas with lower string densities. An explanation for this could be that a larger distance between an event position and its closest DOM increases the relative uncertainty as less photons arrive at this nearest DOM as well as at all remaining DOMs that are even farther apart. So at any given energy, a setup of two events, one with a positions that approaches the maximal distance to its nearest DOM, and one in the immediate surrounding of a detection module, will lead to a certain maximal and minimal relative uncertainty, respectively. And the difference between those two uncertainties increases when the setup is repeated with a larger string distance, as then, the distance between DOMs and thus the maximal distance of an event to any DOM is increased. Also, a generally denser detector lead to any event contained within the detection volume to be detector by more DOMs compared to placing the same event in a detector of lower DOM density.

Moreover, another comparison was undertaken with different rectangular shapes as described in Section 3.2.4 and depicted in Figure 13 and Figure 24. The result is shown in Figure 18b. The cubic detector and that with length of 500 m by 2000 m seem to result in similar relative uncertainties for all energies, with the cubic detector demonstrating slightly lower values for most events. Meanwhile, the detector of 200 m by 5000 m exhibits larger relative uncertainties and a larger spread for all but the lowest-energy event. We would actually expect that a constant string distance as merely a different side length ratio would result in approximately the same relative uncertainty. The most likely explanation is that this detector was by mistake initialized with a larger string distance in one direction compared to the other, as evident when consulting Figure 13. Hence, the total detector volume is also significantly larger for this detector, leading to the increase in absolute uncertainty and spread as already observed in Figure 18a for the square detectors. Still, the slight difference between the other two detector configurations seems to imply that at least for reconstructing the

energy of cascade events, a more compact detector volume is preferred. It would need to be investigated further as this might also be a statistically insignificant effect.
To better compare different detector sizes and their effects, we also need to take into account the advantage of a larger detection area despite the lower string densities causing larger uncertainties on the energy reconstruction. The main advantage of a larger detector is its increased interaction volume. Given an assumed neutrino flux and a uniform interaction probability in the medium, a larger detector results in an increased total number of contained interactions. This, in turn, results in a higher number of potential events that can be detected. However, with a fixed number of detector modules, an increased volume also decreases the sensor density. As a result, a careful balance between detector size and the optical visibility of the target event topologies in the medium is needed.
The effective volume of the different square area detectors for different energies is depicted in Figure 18c. While the effective volume generally increases for larger energies, this effect is most significant for the detector covering the largest area. It fits with our expectation that the effective detection volume for high enough energies encompasses the complete detector as well as a certain volume beyond that.
We can then contrast the achieved effective volumes to the corresponding relative uncertainties of the detector configurations for each energy. If we were to require a resolution of at most 10%, this would allow the largest square detector to reach a lower energy threshold of between 20 TeV and 30 TeV as seen inFigure 18a while increasing the effective volume from approximately $1.5\,\mathrm{km}^3$ to about $6\,\mathrm{km}^3$ when compared to the other two detectors at the same energy range, as presented in Figure 18c. This means the largest detector would detect events in a four times larger volume within surpassing the required resolution threshold. Nevertheless, this means that energies below approximately 20 TeV cannot be reconstructed sufficiently well for this largest detector. Meanwhile, the smallest detector could even detect events of 500 GeV with this uncertainty threshold. Still, its maximally possible effective volume in the total energy range we considered only amounts to less than $1\,\mathrm{km}^3$, while the maximum for the largest detector is approximately $8\,\mathrm{km}^3$ by comparison. Hence, for this comparison of three square configurations, the largest detector might be the preferred option unless the aim is to still be able to reconstruct low-energy events with low uncertainty.
For the other set of detector configurations, the effective volume depending on the energy is then also examined in Figure 18d. It shows the cubic and that of a ratio of 5 : 20 to present coinciding effective volumes, while that of the detector a 2 : 50 ratio has a larger effective volume for all energies. We would expect the effective volume not to vary among the detectors when their volume and string density is equivalent. The reason for the deviation is again that the 2 : 50 detector was initialized with a larger volume than the others, resulting in an effect as observed in Figure 18c for the square detectors.
Apart from this effect, the ratio of detector sides does not appear to have an effect on the effective volume. Hence, as resulting from Figure 18b, the most compact detector might be preferred.

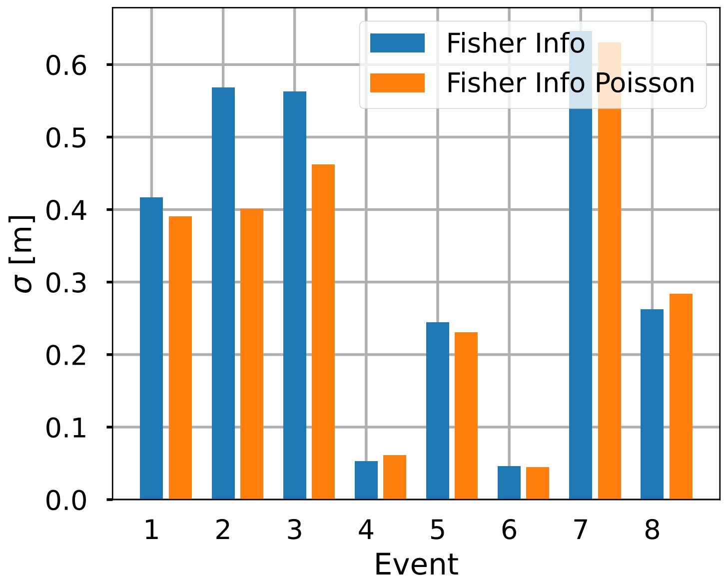

Figure 19: Histogram Comparing Different Methods of Calculating the Position Uncertainty Estimation for Several Cascade Events. The experimental setup is the same as for Figure 15 but applied to the position reconstruction. Additionally, the estimation resulting from the log-likelihood width is not included here as its determination from a log-likelihood of a three-dimensional parameter input is beyond the scope of this thesis. The figure shows the results from both uncertainty estimation methods in agreement within 0.1 m for most events.

5.1.5 Comparison of Position Uncertainty Estimation Methods

We can also compare two different methods of calculating the uncertainty of the position reconstruction. To be precise, we use Equation 16 and Equation 17. After applying the Cramér-Rao bound provided by Equation 7, we obtain two results for the uncertainty estimation σ. It should be noted that the uncertainty estimation from the log-likelihood curve width is more complicated when said log-likelihood depends on three parameters at once. Hence, this method is omitted for the position reconstruction as its realization is beyond the scope of this thesis.

Figure 19 shows that both methods result in similar values. To be precise, for most events the difference is below 0.1 m. The reason for this close correspondence is the same as discussed in Section 5.1.1.

Due to this good agreement of the uncertainty estimations, for the following experiments we use a sample number of 5 and examine only the uncertainty as resulting from Equation 17 unless noted otherwise.

5.1.6 Position Reconstruction Quality

This section discusses the results of the event position reconstruction. The three coordinates for the true and the reconstructed positions of six exemplary events are presented in Table 1. When comparing the values from the reconstruction to the true ones, it is apparent that all dimensions can be reconstructed well, though there are

	-446.54	394.24	345.81	-523.69	364.23	525.99
x_{true} [m]	503.70	-414.27	372.47	-405.09	24.34	391.05
	493.07	-48.19	30.375	375.78	382.24	452.18
	-445.58	389.72	343.76	-524.76	364.44	525.56
x_{reco} [m]	520.30	-415.01	374.84	-403.86	25.10	387.50
	484.73	-49.46	47.33	375.98	379.61	452.47

Table 1: Comparison of True and Reconstructed Event Positions. The three coordinates of the true and the reconstructed values can be compared individually for six exemplary events of random energy and position. For most events, the individual coordinates and hence the full position of the initialization and the reconstruction result coincide within a range of few meters.

some considerable deviations for the y- and z-direction of the first event. This can result from the specific position of that event, with those dimensions approximately at 500 m from the coordinate center. As the detector itself is also centered and extends 500 m to all 6 sides, this means that this first event is situated close to the edge of the detector. When taking into consideration that its x-dimension is also approaching the edge with a value of $x \approx -450\,\text{m}$, we can conclude that the event position is positioned approximately at one corner of the cubic detector. This explains the comparatively worse reconstruction compared to the other events depicted in the table.
To better quantify the reconstruction quality, we compare the distance between the true event position and the reconstructed one to the length of the position vector of the true position, i.e. the distance of the true position to the coordinate center. The result is depicted in Figure 20a for the median of all measurement samples of 50 different events with random energies. We expect that the distance would approach 0 for a good reconstruction, which should be possible for all events contained in the detector. The figure shows that most distances are indeed close to 0.
Still, some events shows a comparatively large spread of distance to the true position as indicated by the error bars. A possible reason for those large values for some event samples could be due to the corresponding events depositing smaller energies. Then, drawing the Poisson-distributed samples has a relatively larger effect on the resulting photon yield measured by the DOMs, so that some samples might only reach half the photon number of another sample of the same cascade event, e.g., one sample resulting in 4 photons arriving at a certain DOM, while the other sample results in 2 photons reaching the same DOM. As discussed for Figure 16, this can lead to some deviation of the reconstructed energy from the true value when the position is known, and vice versa, when the energy is known, it might hence also result in a worse reconstruction and larger uncertainties on the event position.
Additionally, even though all these events are initialized either within the detector volume or in the surrounding border, we need to consider that the events' distance to their nearest DOMs can vary significantly. Hence, for events with a larger distance, we would expect more photons to be absorbed or scattered compared to those initialized close to a detection module. This is turn can also lead to a larger disparity between the true position and the reconstructed one. This behavior might even be aggravated if such an event deposits little energy to begin with, as then more photons might be absorbed and depending on the drawn sample, the total measured photon yield might not even

pass the trigger threshold. So we expect the points with a large distance between those to be an effect of at least one of these two possible reasons.
We then compare the uncertainty resulting from the Fisher Information as calculated from Equation 17 to the position vector of the true event position. The result is depicted in Figure 20b. We expect that the reconstruction uncertainty is related to the distance between the true and the reconstructed position. Figure 20a displays a result for the median and the 18th to 84th percentiles of all samples for each event, while the uncertainty in Figure 20b show a single point for each event, so that the included error bars might obscure some detailed observations. Still, it appears that the general behaviors correspond to one another. For instance, most uncertainties are approximately 0 and the farther the uncertainty departs from 0, the fewer points are present.
As those two previous figures seem to describe a similar behavior, we consequently investigate the distance between true position and reconstructed position divided by uncertainty for the different true positions in Figure 20c. If our observation is correct, we expect to see the points gathering around some constant value for all different true positions. This is confirmed by the figure, which indeed shows the distance per uncertainty to accumulate between 0 and 2 with some deviation to values up to approximately 7 and the percentiles reaching up to about 16. For the point with the largest deviation, we need to take into account that the results for different measurement samples of the same event can vary significantly as depicted by the large error bars. We can observe that the median there is present in the lower end of the percentile spectrum. Hence, the distance between true position and reconstructed position and the uncertainty seem correspond very well to one another.
After these experiments on the position reconstruction for events generated in a volume encompassing the detector volume and an additional border, we turn to investigating events initialized in a fixed interaction volume several times larger than the detector volume. Both means of generating the events in the corresponding volumes are described in Section 4.1.2. With a now wider range of possible event positions, we examine the relation between the reconstruction uncertainty and the distance of the event position to the nearest DOM. For an easier comparison of events, all were initialized with the same high energy of 1 PeV. Figure 20c demonstrates that the uncertainty increases with a larger distance to the closest sensor module. Specifically, it first seems to be approximately constant at a value near 0 up to a minimal DOM distance of about 75 m, after which the uncertainty begins to increase. After reaching a distance of 200 m, the slope becomes significantly larger. It is important to note that the maximal distance of an event contained in the detector to the nearest DOM is approximately 79 m. Hence, all events with a larger minimal distance certainly lie outside the detector. As already discussed before, we expect events outside the detector to result in a larger uncertainty as only a fraction of photons released spherically in the whole solid angle arrive at a detection module. This fraction decreases with a larger distance of the event to the detector. Additionally, as presented in Figure 10, the amount of detectable photons decreases significantly with the distance to the event, with the slope event increasing over the distance. Hence, the figure again corroborates our expectations.

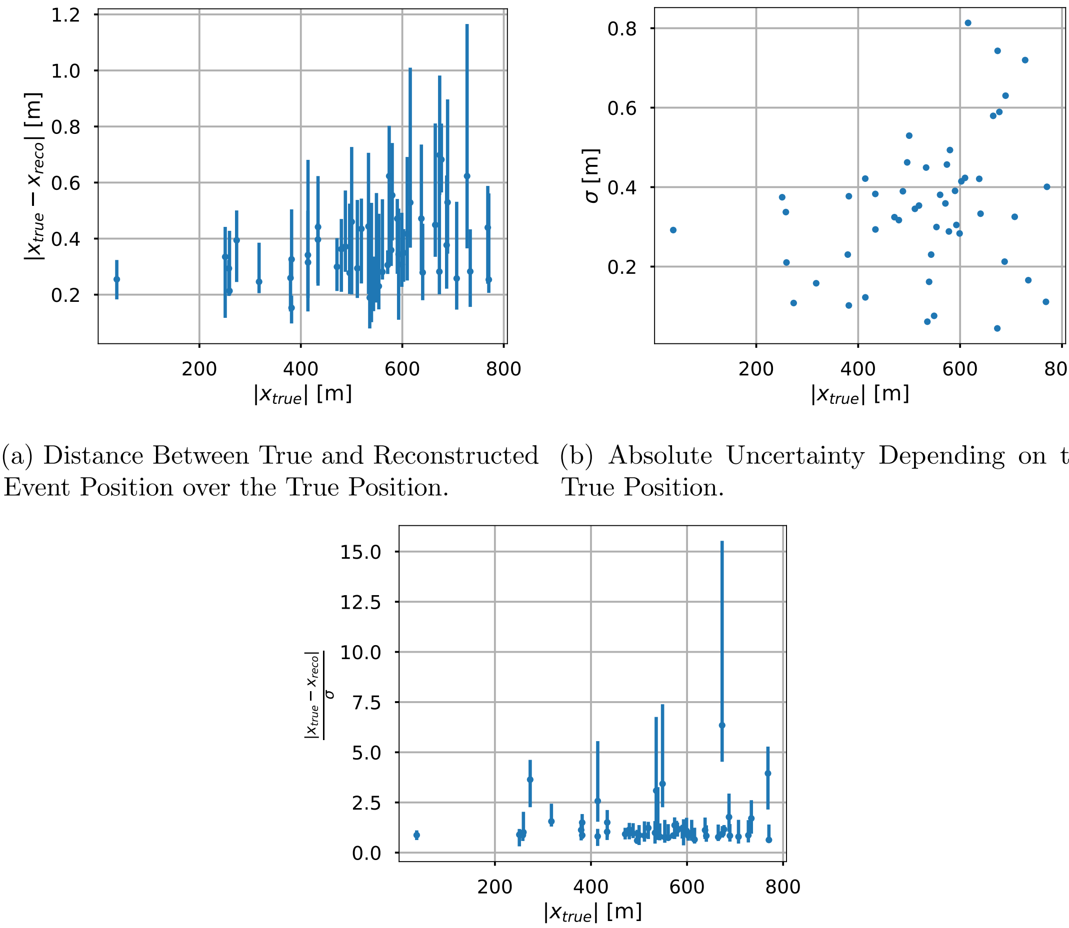

(a) Distance Between True and Reconstructed Event Position over the True Position.

(b) Absolute Uncertainty Depending on the True Position.

(c) Distance Between True and Reconstructed Event Position Divided by Uncertainty over the True Position.

Figure 20: Three Experiments Investigating the Position Reconstruction Quality. All three experiments were conducted for 50 events with random energies and randomized positions within the detector and a surrounding border. Figure 20a depicts the sample median of the distance between reconstructed and true position value over the true position. The error bars correspond to the 18th to 84th percentiles. The figure shows that this deviation from the true position approximates 0 considerably well with all median values below 0.8 m. The spread appears to be larger for events farther outside the detector center, though this effect could be caused by the comparatively low event or sample number. The uncertainty per true event position in Figure 20b is also below 0.8 m for all but one event. Generally, the behavior appears to be similar to that of the position difference. Additionally, said position difference is then divided by the uncertainty to investigate the similarity of their results as presented by Figure 20c. It indeed shows most values grouped between 0 m and 2 m for all positions, indicating a good correspondence between both.

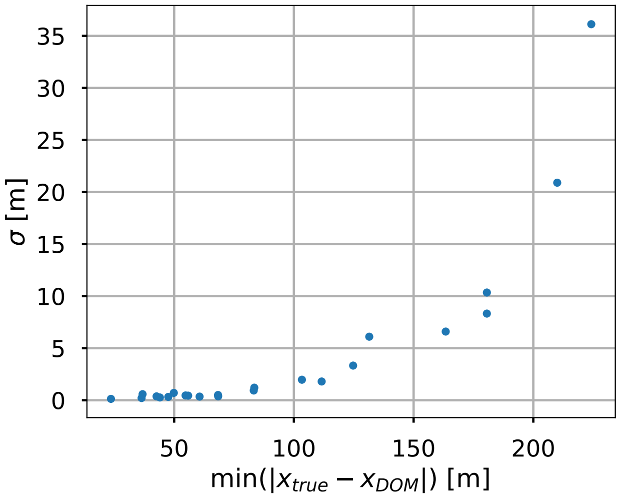

Figure 21: Position Uncertainty over the Distance of the Event to its Nearest DOM. 50 events are initialized within a fixed cubic interaction volume of $8\,\mathrm{km}^3$ centered on the detector center. All event energies are set to $10^6\,\mathrm{GeV}$. The figure shows the uncertainty to increase with a larger distance to the nearest DOM. For a distance smaller than approximately 75 m, the uncertainty seems to be comparatively constant. The maximum possible distance to the nearest DOM an event positioned within the detector can exhibit amounts to 79 m. The uncertainty increase for distances larger than this appears to be approximately linear up to about 200 m, after which the slope consecutively increases further.

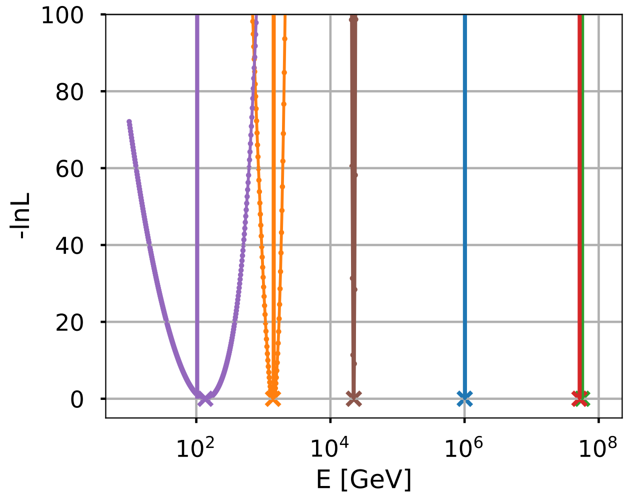

Figure 22: Energy Reconstruction for Several Muon Track Events of Different Energies. The log-likelihood curves minus their minimal values over the energy are depicted as many dots, coinciding well with their corresponding spline fits. The curve minima, denoting the reconstructed energy values, can be compared to the true values, displayed as vertical lines. The figures shows that the reconstructed energies correspond well to the true energies, especially for larger event energies.

5.2 Outlook to Muon Track Events

The analysis for this thesis started out with the cascade events and most time was spent on implementing and examining their reconstruction. Hence, the muon track events are investigated in significantly less detail.
Still, the energy reconstruction is implemented, allowing for a comparison of reconstructed and true energy values. Meanwhile, the uncertainty estimation for all different methods is not realized.
Figure 22 presents the log-likelihood curves after a subtraction of their corresponding curve minima for several muon track events of different energies. The reconstructed energies approximate the true values, with an apparently improving quality for larger energies. This behavior is in agreement with our expectation that higher-energy events deposit higher-energy photons that can reach larger distances and hence more detection modules before being absorbed. This in turn leads to a lower energy reconstruction uncertainty. From the figure, we cannot sufficiently discern whether our expectations regarding the uncertainty are confirmed.
In the future, one could potentially implement the calculation of the energy uncertainty estimation from the log-likelihood curve and utilizing the Fisher Information as presented in Equation 9 and Equation 11. Then the same experiments as discussed in Section 5.1.2 and Section 5.1.3 could be conducted to examine the effects of muon track events of the relative uncertainty or the effective detection volume. Additionally, several detector configurations could again be compared similar to Section 5.1.4.
Furthermore, one could implement a reconstruction of the muon track position as theorized in Section 3.3 and repeat the experiments as presented in Section 5.1.6.
In general, we expect that reconstructing the initial energy is difficult and at the very

least linked to a high uncertainty on the reconstructed energy. The reason for this is that many muon track events emerge before entering the detection volume and continue far beyond it, with only a part of the energy being deposited in the detector. This is especially true for high-energy events. Meanwhile, it is expected that the position of the track trajectory through the detector can be reconstructed very well as many DOMs are involved in the detection process.

6 Conclusion

To summarize, this thesis focused on the reconstruction and analysis of cascade event topologies in water-Cherenkov neutrino telescopes.
The different methods of estimating an uncertainty of the energy reconstruction as presented in Section 3.2.2 were investigated in Section 5.1.1. A comparison showed a good agreement of the results of all three methods. Some deviations are explained by statistical fluctuations. Thereafter, Section 5.1.2 discussed the quality of the energy reconstruction. For one, the reconstructed energy values correspond well to the true energy values, especially when also considering the reconstruction uncertainty. For another , the relative uncertainty decreases for larger true energies as was expected. Additionally, the relative uncertainty displays a similar decrease for an increased number of photons measured by the detector. This is also in agreement with our expectation as the detected photon number depends linearly on the event energy. Section 5.1.3 showed that the effective detection volume increases with higher-energy events as those can be detected even when situated farther away from the detector. After those experiments focusing on a single detector, the investigations are repeated for different detector configurations in Section 5.1.4. The comparisons show that a larger detector with a lower string density generally leads to a larger relative uncertainty, but also an increased effective volume. Both results are in agreement with our expectations. Changing the ratio of the detector side length while maintaining the string density does not appear to have a significant effect on either the relative uncertainty or the effective volume.
Then, different methods of estimating the position reconstruction uncertainty are presented in Section 5.1.5. We observed a very good correspondence of the results. Section 5.1.6 then detailed several experiments investigating the position reconstruction quality. It resulted that the reconstructed position and the true one coincide well. Furthermore, both the distance between those two positions and the reconstruction uncertainty are considerably small. Those two parameters also show a correspondence between their values. Additionally, when considering the uncertainty depending on the distance between an event and its nearest detection module, we observed a consecutive increase for events positioned outside the detector while the other events display the previously noted very small uncertainty.
Finally, Section 5.2 focused on muon track events. The energy reconstruction seemed to work well. The uncertainty on the energy reconstruction is not implemented, just like the track position reconstruction as a whole. Still, the expectation were discussed briefly.
Implementing the remaining part of the muon track reconstruction could be the topic of a potential future work. In the future, one could also implement a simultaneous reconstruction of both the energy and the position. This might be realized for cascade and muon track events. It would allow us to then investigate the effect of the detector configuration with respect to the energy resolution, the position resolution, or a balanced resolution of both. Additionally, more experiments as presented in Section 5.1.4 could be conducted for many different detector shapes. For instance, one could go beyond rectangular surface shapes and even beyond a structured lattice in general. This would allow for a consideration of possible detector geometries that might require a different setup compared to vertically aligned strings.

A Appendix A

A.1 Detector Configurations

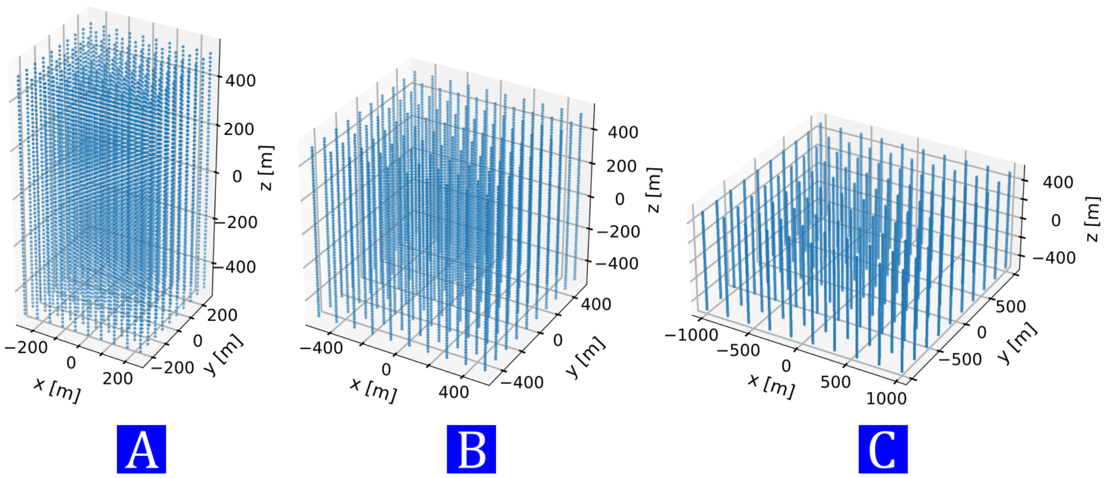

Figure 23: Comparison of Three Detectors with Square Surfaces. All three consist of 10 by 10 strings ordered in a square grid. Configuration A has a side length of 500 m, B one of 1000 m, while C is constrained to a length of 2000 m. The height of 1000 m is equivalent for all three detectors.

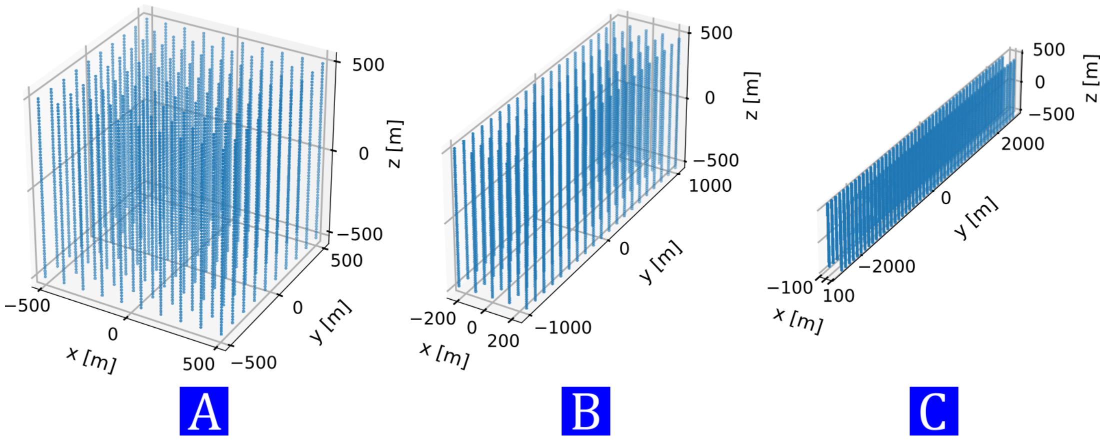

Figure 24: Comparison of Three Rectangular Detectors of Different Side Length Ratios. To keep the string distance the same, the 100 strings in total were placed in the same aspect ratio as the detector side lengths. For A, 10 by 10 strings cover an area of 1000 m by 1000 m. Configuration B consists of 5 by 20 strings in an area of 500 m by 2000 m, effectively doubling one side and halving the other compared to the square detector. Setup C is equipped with 2 by 50 strings covering 200 by 5000 m. Due to a mistake in the initialization of the module positions, the string distances are not equivalent for all three detectors, with the longest detector clearly displaying a larger distance in one dimension compared to the other dimension.

A.2 Calculation for Position Reconstruction

This section presents the complete calculation of Equation 15 omitted in Section 3.2.5. The following equations are needed to calculate the derivative of $\mu(r, E)$ with respect to a space coordinate x_i.

$$\begin{aligned}
\frac{\partial}{\partial x}\frac{1}{\tanh(\frac{x}{c})} &= \frac{-1}{\tanh^2(\frac{x}{c})}\cdot\frac{\partial}{\partial x}\tanh\left(\frac{x}{c}\right)\\
&= \frac{-1}{\tanh^2(\frac{x}{c})}\cdot\frac{1}{\cosh^2(\frac{x}{c})}\cdot\frac{1}{c}\\
&= \frac{-1}{c\tanh^2(\frac{x}{c})\cosh^2(\frac{x}{c})}\\
&= \frac{-1}{c\sinh^2(\frac{x}{c})}
\end{aligned}$$

$$\begin{aligned}
r &= \left(\sum_{i=1}^{3}(x_i - x_{i,\mathrm{DOM}})^2\right)^{\frac{1}{2}}\\
\Rightarrow \frac{\partial}{\partial x_i}r &= \frac{1}{2}\left(\sum_{i=1}^{3}(x_i - x_{i,\mathrm{DOM}})^2\right)^{-\frac{1}{2}}\cdot 2\cdot(x_i - x_{i,\mathrm{DOM}})\\
&= \frac{x_i - x_{i,\mathrm{DOM}}}{r}
\end{aligned}$$

The derivative of the photon yield then amounts to

$$\begin{aligned}
\frac{\partial\mu(r,E)}{\partial x_i} &= \frac{\partial\mu(r,E)}{\partial r}\frac{\partial r}{\partial x_i}\\
&= \frac{\partial}{\partial r}\left(n_0 A\frac{1}{4\pi}e^{\frac{-r}{\lambda_p}}\frac{1}{\lambda_c r\tanh\left(\frac{r}{\lambda_c}\right)}\cdot\frac{E\,[\mathrm{GeV}]}{3\cdot 10^5\,\mathrm{GeV}}\right)\frac{\partial r}{\partial x_i}\\
&= \frac{n_0 A}{4\pi\lambda_c}\frac{E\,[\mathrm{GeV}]}{3\cdot 10^5\,\mathrm{GeV}}\frac{\partial}{\partial r}\left(e^{\frac{-r}{\lambda_p}}\frac{1}{r}\frac{1}{\tanh\left(\frac{r}{\lambda_c}\right)}\right)\frac{\partial r}{\partial x_i}\\
&= \frac{n_0 A}{4\pi\lambda_c}\frac{E\,[\mathrm{GeV}]}{3\cdot 10^5\,\mathrm{GeV}}\left(e^{\frac{-r}{\lambda_p}}\left(\frac{1}{-\lambda_p}\right)\frac{1}{r}\frac{1}{\tanh\left(\frac{r}{\lambda_c}\right)}\right.\\
&\quad\left.+\,e^{\frac{-r}{\lambda_p}}\left(\frac{-1}{r^2}\right)\frac{1}{\tanh\left(\frac{r}{\lambda_c}\right)} + e^{\frac{-r}{\lambda_p}}\frac{1}{r}\frac{-1}{\lambda_c\tanh^2(\frac{r}{\lambda_c})\cosh^2(\frac{r}{\lambda_c})}\right)\frac{\partial r}{\partial x_i}\\
&= -\frac{n_0 A}{4\pi\lambda_c}\frac{E\,[\mathrm{GeV}]}{3\cdot 10^5\,\mathrm{GeV}}e^{\frac{-r}{\lambda_p}}\frac{1}{r}\frac{1}{\tanh\left(\frac{r}{\lambda_c}\right)}\left(\frac{1}{\lambda_p}+\frac{1}{r}+\frac{1}{\lambda_c\tanh(\frac{r}{\lambda_c})\cosh^2(\frac{r}{\lambda_c})}\right)\frac{\partial r}{\partial x_i}\\
&= -\mu(r,E)\cdot\left(\frac{1}{\lambda_p}+\frac{1}{r}+\frac{1}{\lambda_c\tanh(\frac{r}{\lambda_c})\cosh^2(\frac{r}{\lambda_c})}\right)\frac{\partial r}{\partial x_i}\\
&\overset{\frac{\partial r}{\partial x_i}=\frac{x_i - x_{i,\mathrm{DOM}}}{r}}{=} -\mu(r,E)\cdot\left(\frac{1}{\lambda_p}+\frac{1}{r}+\frac{1}{\lambda_c\tanh(\frac{r}{\lambda_c})\cosh^2(\frac{r}{\lambda_c})}\right)\frac{x_i - x_{i,\mathrm{DOM}}}{r}.
\end{aligned}$$

Bibliography

Aartsen, M G, R Abbasi, M Ackermann, J Adams, et al. (Mar. 2014). "Energy reconstruction methods in the IceCube neutrino telescope". In: *Journal of Instrumentation* 9.03, P03009–P03009. ISSN: 1748-0221. DOI: 10.1088/1748-0221/9/03/p03009. URL: http://dx.doi.org/10.1088/1748-0221/9/03/P03009.

Abbasi, R., Y. Abdou, T. Abu-Zayyad, J. Adams, et al. (June 2010). "Calibration and characterization of the IceCube photomultiplier tube". In: *Nuclear Instruments and Methods in Physics Research Section A: Accelerators, Spectrometers, Detectors and Associated Equipment* 618.1-3, 139–152. ISSN: 0168-9002. DOI: 10.1016/j.nima.2010.03.102. URL: http://dx.doi.org/10.1016/j.nima.2010.03.102.

Bailey, J, K Borer, F Combley, H Drumm, et al. (July 1977). "Measurements of relativistic time dilatation for positive and negative muons in a circular orbit". In: *Nature* 268. DOI: 10.1038/268301a0.

Bellini, G., L. Ludhova, G. Ranucci, and F. L. Villante (2014). "Neutrino Oscillations". In: *Advances in High Energy Physics* 2014, 1–28. ISSN: 1687-7365. DOI: 10.1155/2014/191960. URL: http://dx.doi.org/10.1155/2014/191960.

Brent, Richard P. (1973). *Algorithms For Minimization Without Derivatives*. Prentice Hall. ISBN: 0-486-41998-3.

Byrd, Richard H., Peihuang Lu, Jorge Nocedal, and Ciyou Zhu (1995). "A Limited Memory Algorithm for Bound Constrained Optimization". In: *SIAM J. Sci. Comput.* 16, pp. 1190–1208.

Cramér, Harald (1946). *Mathematical Methods of Statistics*. Princeton University Press. ISBN: 9780691005478.

Dey, U. K. (Oct. 2024). "Cosmic neutrino background: a minireview". In: *Eur. Phys. J. Spec. Top.* 233, 2149–2161. DOI: 10.1140/epjs/s11734-024-01101-w. URL: https://doi.org/10.1140/epjs/s11734-024-01101-w.

Fletcher, R. (1987). *Practical Methods of Optimization*. John Wiley & Sons. ISBN: 9780471915478. DOI: 10.1002/9781118723203.

Giganti, C., S. Lavignac, and M. Zito (Jan. 2018). "Neutrino oscillations: The rise of the PMNS paradigm". In: *Progress in Particle and Nuclear Physics* 98, 1–54. ISSN: 0146-6410. DOI: 10.1016/j.ppnp.2017.10.001. URL: http://dx.doi.org/10.1016/j.ppnp.2017.10.001.

Hamamatsu Photonics (n.d.). *Photomultiplier Tubes - Basics and Applications*. https://www.hamamatsu.com/content/dam/hamamatsu-photonics/sites/documents/99_SALES_LIBRARY/etd/PMT_handbook_v4E.pdf. [Online; accessed 06-July-2026].

IceCube Collaboration (n.d.). *IceCube*. https://icecube.wisc.edu/science/icecube/. [Online; accessed 19-June-2026].

— (Nov. 2013). "Evidence for High-Energy Extraterrestrial Neutrinos at the IceCube Detector". In: *Science* 342.6161. ISSN: 1095-9203. DOI: 10.1126/science.1242856. URL: http://dx.doi.org/10.1126/science.1242856.

IceCube-Gen2 Collaboration (2023). *The next generation neutrino telescope: IceCube-Gen2*. arXiv: 2308.09427 [astro-ph.HE]. URL: https://arxiv.org/abs/2308.09427.

Katz, U.F. and Ch. Spiering (2012). "High-energy neutrino astrophysics: Status and perspectives". In: *Progress in Particle and Nuclear Physics* 67.3, pp. 651–704. ISSN: 0146-6410. DOI: https://doi.org/10.1016/j.ppnp.2011.12.001. URL: https://www.sciencedirect.com/science/article/pii/S0146641011001189.

King-Klemperer, Alisa for the IceCube Collaboration (Feb. 12, 2026). *The IceCube Neutrino Observatory gets a major upgrade beneath the ice*. https://icecube.wisc.edu/news/press-releases/2026/02/the-icecube-neutrino-observatory-gets-a-major-upgrade-beneath-the-ice/. [Online; accessed 05-July-2026].

KM3NeT Collaboration (n.d.). *The neutrino detectors*. https://www.km3net.org/research/detector/. [Online; accessed 04-July-2026].

— (2025). "Observation of an ultra-high-energy cosmic neutrino with KM3NeT". In: *Nature* 638, 376–382. URL: https://doi.org/10.1038/s41586-024-08543-1.

Lin, Joshua and Bruno Scheihing-Hitschfeld (2026). *Quantum and Thermal Fluctuations of Cherenkov Radiation from HQET*. arXiv: 2603.06784 [hep-ph]. URL: https://arxiv.org/abs/2603.06784.

Lista, Luca (Jan. 2023). *Statistical Methods for Data Analysis: With Applications in Particle Physics*. ISBN: 978-3-031-19933-2. DOI: 10.1007/978-3-031-19934-9.

Mayer, Benedikt (2025). "Development of a Recurrent Neural Network for optimizing the muon simulation efficiency in IceCube". Friedrich-Alexander Universität Erlangen-Nürnberg, Erlangen Center for Astroparticle Physics.

Navas, S., C. Amsler, T. Gutsche, C. Hanhart, et al. (Aug. 2024). "Review of Particle Physics". In: *Phys. Rev. D* 110 (3), p. 030001. DOI: 10.1103/PhysRevD.110.030001. URL: https://link.aps.org/doi/10.1103/PhysRevD.110.030001.

P-ONE Collaboration (2019). *The Pacific Ocean Neutrino Telescope (P-ONE)*. https://www.pacific-neutrino.org/p-one. [Online; accessed 19-June-2026].

Poisson, Siméon-Denis (1837). *Recherches sur la probabilité des jugements en matière criminelle et en matière civile*. Bachelier.

Rädel, Leif and Christopher Wiebusch (Oct. 2012). "Calculation of the Cherenkov light yield from low energetic secondary particles accompanying high-energy muons in ice and water with Geant4 simulations". In: *Astroparticle Physics* 38, 53–67. ISSN: 0927-6505. DOI: 10.1016/j.astropartphys.2012.09.008. URL: http://dx.doi.org/10.1016/j.astropartphys.2012.09.008.

Salas, Pablo F. de, Stefano Gariazzo, Olga Mena, Christoph A. Ternes, and Mariam Tórtola (Oct. 2018). "Neutrino Mass Ordering from Oscillations and Beyond: 2018 Status and Future Prospects". In: *Frontiers in Astronomy and Space Sciences* 5. ISSN: 2296-987X. DOI: 10.3389/fspas.2018.00036. URL: http://dx.doi.org/10.3389/fspas.2018.00036.

Schneider, Judith (2024). “Characterization of the mDOM light detection and signal processing system for the IceCube Upgrade”. PhD thesis. Friedrich-Alexander Universität Erlangen-Nürnberg, Erlangen Center for Astroparticle Physics.

Scott, Douglas (2024). *The Cosmic Neutrino Background*. arXiv: 2402.16243 [astro-ph.CO]. URL: https://arxiv.org/abs/2402.16243.

Tamm, I. E. and I. M. Frank (1967). “Kogerentnoe izluchenie bystrogo elektrona v srede”. In: *Usp. Fiz. Nauk* 93.10, pp. 388–393. DOI: 10.3367/UFNr.0093.196710o.0388. URL: https://ufn.ru/ru/articles/1967/10/o/.

Vitagliano, Edoardo, Irene Tamborra, and Georg Raffelt (Dec. 2020). “Grand unified neutrino spectrum at Earth: Sources and spectral components”. In: *Reviews of Modern Physics* 92.4. ISSN: 1539-0756. DOI: 10.1103/revmodphys.92.045006. URL: http://dx.doi.org/10.1103/RevModPhys.92.045006.

Declaration of Originality

I, Franziska Kirchner, student registration number: 22669607, hereby confirm that I completed the submitted work independently and without the unauthorized assistance of third parties and without the use of undisclosed and, in particular, unauthorized aids. This work has not been previously submitted in its current form or in a similar form to any other examination authorities and has not been accepted as part of an examination by any other examination authority.

Where the wording has been taken from other people's work or ideas, this has been properly acknowledged and referenced. This also applies to drawings, sketches, diagrams and sources from the Internet.

In particular, I am aware that the use of artificial intelligence is forbidden unless its use an aid has been expressly permitted by the examiner. This applies in particular to chatbots (especially ChatGPT) and such programs in general that can complete the tasks of the examination or parts thereof on my behalf. As such, this work has been completed without the use of artificial intelligence.

Any infringements of the above rules constitute fraud or attempted fraud and shall lead to the examination being graded "fail" ("nicht bestanden").

Erlangen, 07.07.2026

Place, Date

Signature